Visible Light Communication System Evaluations With Integrated Hardware and Optical Parameters

Li Zhou, Cheng-Xiang Wang, *Fellow, IEEE*, Ahmed Al-Kinani, and Wen-Sheng Zhang, *Member, IEEE*

Abstract—**Visible light communication (VLC) is an emerging nascent research area having enormous application prospects. Efficient evaluation methods are critical requirements for implementing high-performance VLC systems. Most research just focus on system analyses from optical channels, modulation methods, or communication theories. However, the basic theoretical analyses of the relationships between hardware circuit current energy and optical power are absent. This paper makes up for this deficiency. Based on a general VLC communication scenario, we theoretically analyze the transferring procedures between circuit current energy and optical power. The current energy transferring calculation model (CETCM) and CET parameters are proposed for the first time. The peak current energy response, current energy gain, threshold of optical power transferring distance, and current signal-to-noise ratio can be calculated by the CETCM and CET parameters. Experiments show that they can comprehensively reflect the communication characteristics of practical VLC system, and are quite important and valuable for VLC system evaluations, implementations, and optimizations.**

Index Terms—**VLC, hardware circuit, current energy, optical power.**

I. INTRODUCTION

VISIBLE light communication (VLC) is an emerging communication research area focusing on last ten-meter

L. Zhou is with the School of Microelectronics, Shandong University, Jinan 250100, China (e-mail: zhou_li@sdu.edu.cn).

C.-X. Wang is with the Institute of Sensors, Signals and Systems, School of Engineering and Physical Sciences, Heriot-Watt University, Edinburgh EH14 4A S, U.K., and also with the Shandong Provincial Key Laboratory of Wireless Communication Technologies, School of Information Science and Engineering, Shandong University, Qingdao 266237, China (e-mail: cheng-xiang.wang@hw.ac.uk).

A. Al-Kinani was with the Institute of Sensors, Signals and Systems, School of Engineering and Physical Sciences, Heriot-Watt University, Edinburgh EH14 4AS, U.K. He is now with the Iraqi Ministry of Communications, Baghdad, Iraq (e-mail: aa1304@hw.ac.uk).

W.-S. Zhang is with the Shandong Provincial Key Laboratory of Wireless Communication Technologies, School of Information Science and Engineering, Shandong University, Qingdao 266237, China (e-mail: zhangwensheng@sdu.edu.cn).

Color versions of one or more of the figures in this paper are available online at http://ieeexplore.ieee.org.

Digital Object Identifier 10.1109/TCOMM.2018.2826002

communication technology with low-cost, energy-efficient, and high-performance requirements [1], [2]. VLC offers some superior aspects such as unlicensed bandwidth, friendly environment, free electromagnetic interference, and secure communications. VLC system design and evaluation are complex because circuit and optical parameters are involved simultaneously with complex signal interferences. IEEE Committee has published VLC system design standard of IEEE 802.15.7 [3], which leaves a much broad design space for VLC system improvements.

Many papers reported high-performance VLC system implementations. Chi et al. implemented a series of VLC systems with pre-equalization methods. A 2.08-Gbit/s VLC transmission over 1m free-space distance was implemented with power exponential software pre-equalization based on a phosphorescent white LED [4]. A 8-Gb/s VLC system was experimentally achieved over a 1-m indoor free-space transmission with a hybrid post equalizer and the red blue green yellow light-emitting diode (RBGY LED) for four-wavelength multiplexing [5]. A gigabit per second VLC transmission over 80-cm free space was realized with a constant-resistance symmetrical bridged-T amplitude equalizer based on a RGB LED [6]. A 2.0-Gb/s visible light link over 1.5-m free-space transmission was realized based on a single commercially available phosphorescent white light-emitting diode [7], and with red-green-blue (RGB) source lights [8]. Che et al. [9] realized system-on-chip (SoC) based 266 kb/s data rate VLC systems with multiple dimming levels and a switching boost LED driver with an on-chip power MOSFET. Haigh et al. [10] implemented a VLC system based on a low bandwidth polymer light-emitting diode (LED) device with 10-Mb/s bit rate. Hsu et al. [11] implemented a Gb/s VLC transmission by hardware pre-equalization circuit. Sewaiwar et al. [12] designed a VLC system with RGB LEDs and on-off keying (OOK) modulation scheme. Fahs et al. [13] implemented a 2.5 Gb/s VLC system over 12 m link distance with laser diode source. Although these presented systems have high-performance, they are lack of theoretical analyses of VLC systems. Theoretical analyses needs to be illustrated in VLC system evaluations.

The initial theoretical analysis started from VLC channel modeling. Afgani et al. [14] presented a VLC channel model based on an infrared optical channel model [15]. It was demonstrated theoretically that the high peak-to-average ratio (PAR) in OFDM can be exploited constructively in VLC to intensity modulate LEDs. The channel model and system capacity considering multi-input-multi-output (MIMO) schemes are further improved in [16]–[18]. Chen and Jiang [19] gave an adaptive statistical Bayesian minimum mean square error

channel model, and proposed optical orthogonal frequency division multiplexing. He *et al.* [20] proposed an invertible channel matrix model. High-rank channel matrix was proposed in [21] and [22]. Wei *et al.* [23] presented a cubic Rx system model with five photodetectors (PD) to solve the problem of an ill-conditioned channel matrix problem, and achieved 14.5-bit/s/Hz performance. Our research team introduced a geometry-based stochastic channel model for VLC channels [24], [25]. These channel models focus on the channel behavior either with different numbers of transmitter (Tx) or receiver (Rx), or with PD field of view (FOV) characteristics. They did not analyze the whole VLC system behaviors combined with other components.

Therefore, some papers started to model VLC systems combined with various channel modulation or coding schemes [26], [27]. Haas *et al.* [14], [28] firstly investigated the impact of OFDM modulation method on the performance of VLC systems. Some improved MIMO-OFDM VLC system were proposed to increase VLC systems performance in [23], [29], and [30]. Yang *et al.* [31] presented asymmetrically clipped optical OFDM (ACO-OFDM) and OOK modulation schemes to support the different qualities of service with high spectral efficiency. Yang *et al.* [32] evaluated VLC systems with an enhanced direct-current O-OFDM (DCO-OFDM) modulation method, and introduced a piecewise function with adaptive slopes according to the required optical power. Mossaad *et al.* [33] proposed a spatial optical OFDM (SO-OFDM) modulation method, and compared the performance with DCO-OFDM method. Feng *et al.* [34] researched a linear two steps pre-coding method to improve VLC system performance.

The above VLC modulation or coding schemes are only software-based modeling. They did not consider the critical hardware circuits factors in practical VLC systems. However, the relationship between circuit parameters and optical power is quite important for hardware system evaluations. Liu *et al.* [35] considered the Tx voltage impact on the OOK signal waveform, and gave the model of photo-multiplier tube (PMT) Rx, which is impractical in normal VLC system. While Liu only used the Gaussian distributions for modeling VLC channels, which is far from rigorous. Chun *et al.* [17] analyzed VLC systems considering the relationship between optical spectrum power and illumination level of Tx, but Chun did not put the analysis into the whole VLC system transmission process. Only bandwidth and data-rate examinations are far from enough for the VLC system evaluation. Nuwanpriya *et al.* [21] analyzed VLC systems with multiple PDs by pyramid or hemispheric angle orientations. Channel capacity and BER performance were evaluated for practical experiments. However only consider the PDs angle or orientation is far from enough for practical VLC system design. Yin *et al.* [36] proposed a VLC system model with the direct-current (DC) bias I_{DC} added to LED. The transmitting optical power was estimated as linear with I_{DC}. However, the nonlinear DC regeneration relationship of PD was not considered. Therefore, only focusing on analyzing channel characteristics, or only evaluating device characteristics, could not fully reflect the comprehensive VLC system working situations.
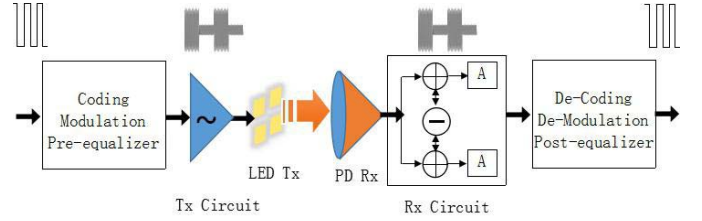

Fig. 1. A general VLC system built up based on hardware circuit.

In the previous work, the transformation between hardware circuit energy and radiant optical power was rarely mentioned. The MIMO VLC system performance is also seldom analyzed based on hardware circuit characteristics.

The purpose of this paper is to fill the above research gaps, i.e., to theoretically evaluate the performance of the whole VLC system by exploring the potential relationship between hardware circuit variables, devices characteristic parameters, and light luminance parameters. The rest of this paper is organized as follows. Section II presents the theoretical analyses of Txs, optical communication channel, and Rxs. The CETCM model is proposed based on the analyses. Detailed parameter definitions of CET parameters are given in Section III. Section IV provides the experiment results. Conclusions are given in Section V.

II. VLC SYSTEM ANALYSES WITH INTEGRATED HARDWARE AND OPTICAL PARAMETERS

General components of VLC systems include VLC signal generation, Tx with LED devices, optical wireless channel, Rx with PD, and signal reproduction. The Tx LED devices are drived by DC bias current with alternating current (AC) current to represent signals. The Tx electric current energy is transferred into optical power, transmitted wirelessly, and then detected by the PD, converted into current energy again which is processed by Rx hardware circuit to reproduce transmitted signals. This is a tightly linked system. All these key steps are related with hardware circuit current energy and optical power, as shown in Fig. 1.

Inherent relationships exist among circuit components and optical parameters, which determine the VLC system performance and efficiency. Theoretical analyses are needed to get the comprehensive picture of the VLC system working scenarios. Key geometric variables and measured parameters of hardware circuit and optical devices used in the paper are listed in Table I for clarity. The analyses process starts from signal samples generation in Txs to the samples regeneration in Rxs, together with optical channel transmitting. A general MIMO VLC system scenario and components are shown in Fig. 2. The communication space is a room with (X, Y, Z) size. Four roof LED Txs are at position $(X/4, Y/4, Z)$, $(3X/4, Y/4, Z)$, $(X/4, 3Y/4, Z)$, and $(3X/4, 3Y/4, Z)$ respectively. The Rxs are on the plane with height H over the floor. Typical Rx positions are at position $(1, 1, H)$, $(X/4, Y/4, H)$, $(X/2, Y/2, H)$, and (X, Y, H).

A. Tx Analyses

Usually, Tx LED is a device driven by hardware circuit current. LED has many advantages over incandescent light

TABLE I

SYMBOLS AND VARIABLES

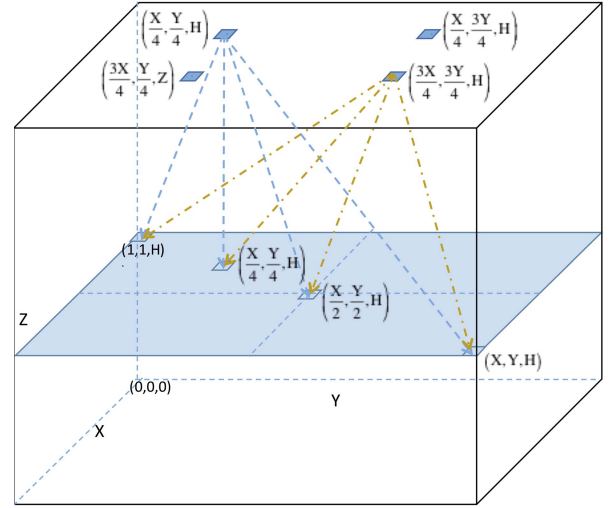| Parameter	VLC system parameter definition
λ	Wavelength of light
$I_{Tx}(t)$, $V_{Tx}(t)$	Tx LED supply current (forward current) and supply voltage (forward voltage), respectively
I_{Tx_H}	Tx LED max supply current
$P_{Tx}(\lambda)$, $P_{Tx}(I)$	Optical Tx power as a function of λ or I_{Tx}, usually given by normalized value
P_{Tx_MI}, P_{Tx_MW}	Maximum value of $P_{Tx}(I)$ and $P_{Tx}(\lambda)$
b_0, b_1, b_2	DC, linear and second-order nonlinearity coefficient of function $P_{Tx}(I)$, respectively
p_an, p_bn, p_cn	$P_{Tx}(\lambda)$ function coefficient
η	Power efficiency ratio of Tx optical power to Tx supply power
$I_{Rx}(t)$	Rx photodiode output electric current
$P_{Rx}(t;\lambda)$	Rx optical power
$Z(\lambda)$	PD A/W response, the photocurrent generated per unit incident optical power, varying with wavelength
z_an, z_bn, z_cn	$Z(\lambda)$ function coefficient
d, d_0	General distance and Line-of-Sight (LoS) distance between the Tx and Rx, respectively
c	Speed of light
r	Radius of the Rx aperture
FOV	Rx PD angle range
ψ	Angle between the Tx axis and Tx/Rx line
Ψ_{FOV}, $\Psi_{\frac{FoV}{2}}$	Maximum Rx FOV incidence angle and half-power angle
ϕ	Tx viewing angle
$\phi_{\frac{1}{2}}$	Semi-angle at half luminance
$R(\phi)$	Radiation profile of light source
ω	Rx solid angle as observed from the Tx
m	Order of Lambertian emission
A_{Rx}	Rx PD detecting physical area
$A_{Rx}^{eff}(\psi)$	Effective signal-collection area of PD
$g(\psi)$	Rx optical concentrator gain before PD
$T_s(\psi)$	Signal transmission functionality of Rx optical filter before PD
n	Receive refractive index of the optics material
$\delta(t)$	Light transmission response delta function
$rect(x)$	Light transmission incident view function
N_r	Number of reflection surface
Γ_n^k	Optical power of reflected ray after the kth bounce from the nth LED
$\rho(\lambda)$	Spectral reflectance coefficient varying as a function of wavelength

Fig. 2.   A general VLC system scenario with Txs and Rxs under analyses.

published LED device characteristics of world's leading LED manufactories are studied in our research. Usually, only normalized values are used in the published curves of $P_{Tx}(I)$, and the curve shapes from different manufacturers are similar. The $P_{Tx}(\lambda)$ has the same situation. Figs. 3 (a) and (b) show the NCSWE17A LED device $P_{Tx}(\lambda)$ and $P_{Tx}(I)$ curves published by Nichia Ltd. [39]. Figs. 3 (c) and (d) show the C513A high intensity LED device $P_{Tx}(\lambda)$ and $P_{Tx}(I)$ curves published by CREE Ltd. [40].

The instantaneous optical power value $P_{Tx}(I)$ changes with driving current I_{Tx}, multiplied by its maximum value P_{Tx_MI}. The quadratic polynomial functional expression is proved to be a fair description of $P_{Tx}(I)$ [41] [42], i.e., $P_{Tx}(I) = P_{Tx\_MI} \cdot (b_2 I_{Tx}^2 + b_1 I_{Tx} + b_0)$. When $I_{Tx} = 0$, there is no supply current, $P_{Tx}(I) = 0$. So, $b_0 = 0$. When I_{Tx} changes from 0 mA to I_{Tx_H} mA, $P_{Tx}(I)$ changes from 0 to P_{Tx_MI}. The fitted quadratic polynomial function curves are shown for each LED device in Figs. 3 (b) and (d) with red solid-line respectively. Compared with published curves in blue dash-line, the quadratic polynomial functions have enough accuracy, and are used in this paper to model LED $P_{Tx}(I)$ response functions.

The LED supply hardware circuit power is $I_{Tx} \cdot V_{Tx}$. The power efficiency ratio between Tx optical power and Tx supplied power is $\eta = P_{Tx}(I)/(I_{Tx} \cdot V_{Tx})$ [43]. Then, $\eta \cdot V_{Tx} = P_{Tx\_MI}(b_2 I_{Tx} + b_1)$. The $P_{Tx}(\lambda)$ generally has two waveform peak response amplitudes [44]. One appears around blue wavelength with comparable sharp pulse. Another peak appears around green wavelength with comparable smooth shape. Each peak waveform is with a second-order exponential like waveform. So combining the two peak waveform, the $P_{Tx}(\lambda)$ curve can be fitted by a second-order exponential function as

$$P_{Tx}(\lambda) = p\_a1 \cdot \exp\left(-\frac{\lambda - p\_b1}{p\_c1}\right)^2 + p\_a2 \cdot \exp\left(-\frac{\lambda - p\_b2}{p\_c2}\right)^2. \quad (1)$$

Red solid-line curves, as the fitting curves shown in Figs. 3 (a) and (c), match well with the blue dot-line curves published by

sources because of lower energy consumption, longer lifetime, smaller size, and faster switching. It is powerful enough for the advanced VLC communication technologies. Development of white-LED (WLED) rapidly matched and overtook the efficacy of standard incandescent and fluorescent lighting [37]. There are three main methods to produce white light from LED, i.e., color mixing by separately RGB LED devices, near ultraviolet (UV) or UV LED with RGB phosphor, and blue LED with yellow phosphor which is the most commonly used in VLC systems [38]. The last type is also used in this paper for the convenience of modeling derivation. While the analysis methods could be applied to other similar LED types.

Two curves are always clearly measured and published by LED device manufactories. One is the relationship between $P_{Tx}(I)$ and I_{Tx}. The other is the relationship between $P_{Tx}(\lambda)$ and λ. The unit of $P_{Tx}(\lambda)$ is Watts/nm [2]. In order to improve the conviction of data used in the paper, most
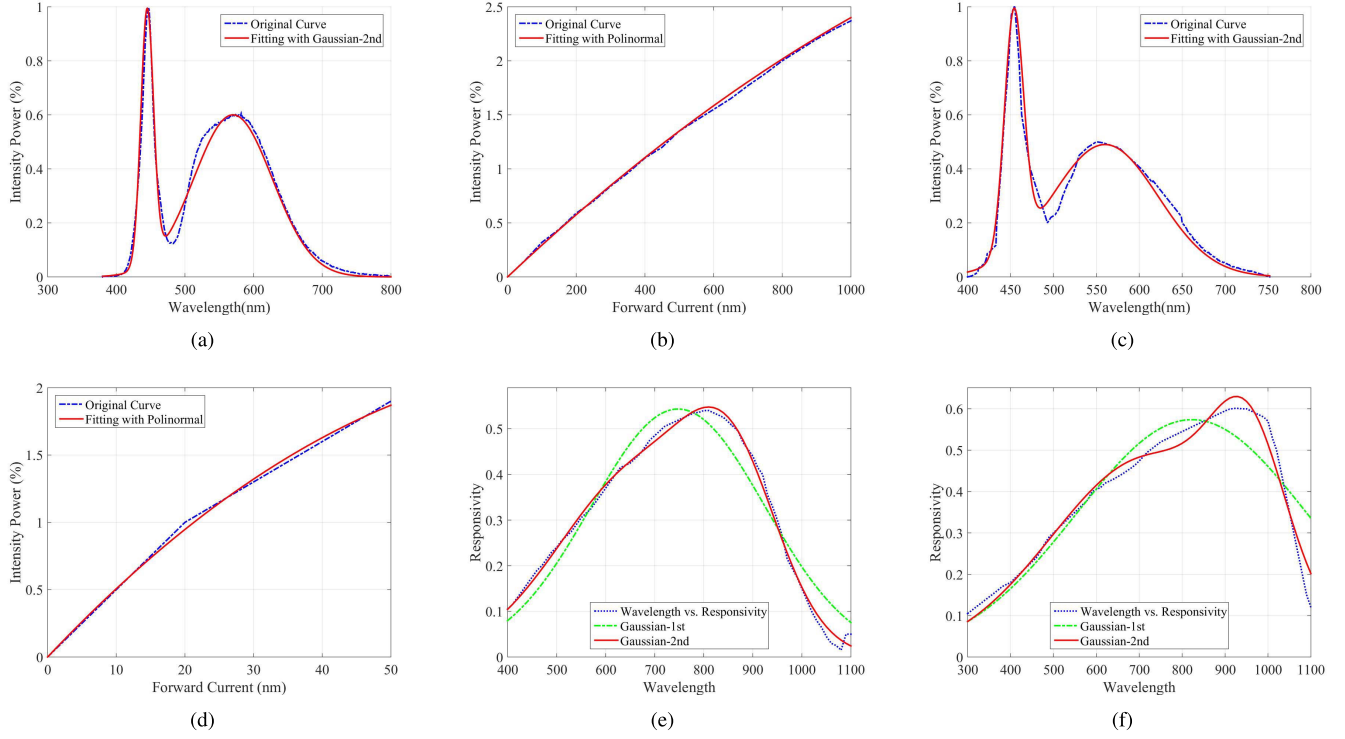
Fig. 3. The LED device responses of $P_{Tx}(\lambda)$, $P_{Tx}(I)$ and the PD responses of $Z(\lambda)$. (a) and (b) are the NCSWE17A LED device response curves from Nichia Ltd. (c) and (d) are the C513A LED device response curves from CREE Ltd. (e) and (f) are the PD response curves of LSSPD-1.2 from Lightsensing Ltd. and 602PX from First Sensor Ltd.

manufactures [39], [40]. The total optical power is calculated by taking the integral of all instantaneous response values over all spectrums, and is equal to $P_{Tx}(I)$. So, there is

$$P_{Tx\_MI} \cdot \left(b_2 I_{Tx}^2 + b_1 I_{Tx} \right) = \eta V_{Tx} I_{Tx}$$
$$= P_{Tx\_MW} \cdot \int_\lambda P_{Tx}(\lambda) d\lambda. \tag{2}$$

Define $P_{Tx\_M} = P_{Tx\_MI}/P_{Tx\_MW}$ as maximum value coefficient. Then, it can be derived that

$$\int_\lambda P_{Tx}(\lambda) d\lambda = P_{Tx\_M} \cdot I_{Tx} \left(b_2 I_{Tx} + b_1 \right)$$
$$= \eta V_{Tx} I_{Tx}/P_{Tx\_MW}, \tag{3}$$

$$I_{Tx} = \frac{-b_1 + \sqrt{b_1^2 + \frac{4b_2}{P_{Tx\_M}} \int_\lambda P_{Tx}(\lambda) d\lambda}}{2b_2}$$
$$= \frac{P_{Tx\_MW}}{\eta V_{Tx}} \int_\lambda P_{Tx}(\lambda) d\lambda = \frac{1}{b_2} \left[\frac{\eta V_{Tx}}{P_{Tx\_MI}} - b_1 \right], \tag{4}$$

and $\int_\lambda P_{Tx}(\lambda) d\lambda + \frac{b_1^2 \cdot P_{Tx\_M}}{4b_2} \geq 0$. Although WLED with phosphor is studied in this paper, other LED types also have specific diagrams for both $P_{Tx}(I)$ and $P_{Tx}(\lambda)$. The analyses methods can also be used to simulate other Tx devices.

The instantaneous value of received optical power is the $P_{Rx}(t; \lambda)$ which changes with the spectrum wavelength and time. The $P_{Rx}(t; \lambda)$ definitely affects the Rx circuit current responses. The intensity modulation and direct detection (IM/DD) concept proposed by Kahn and Barry [15]

is used here to model the Tx and Rx behaviors. The Tx Lambertian radiant intensity $R(\phi) = \frac{m+1}{2\pi} \cos^m(\phi)$, unit is 1/sr. Here, m is Lambertian emission order, $m = (-\ln 20)/\left[\ln \left(\cos \left(\Phi_{\frac{1}{2}} \right) \right) \right]$. It depends on semi-angle at half radiation luminous intensity $\Phi_{\frac{1}{2}}$. If $\Phi_{\frac{1}{2}} = 60°$, $m = 1$ [45].

The Tx driving circuit needs to be designed to match communication frequency and non-linear parameters of LED device. Define T_p as the signal period within which the Rx current is assumed to recover to zero between adjacent pulses, transmitted signal bit rate is $R_b = 1/T_p$, rising time τ_r and falling time τ_f are the time difference between the 10% and 90% points of the driving current, τ_c is the equivalent RC time constant of Tx driving circuit, the minority carrier lifetime of LED device is τ_m which determines the LED device transient and frequency behaviors. The total LED junction capacitance C_j is the sum of its diffusion capacitance C_d and its depletion capacitance C_s, i.e. $C_j = C_d + C_s$ [46]. The C_d affects the minority carrier lifetime τ_m, which further determines the LED transmission speed between current energy and optical energy [58]. As proved in [46], considering LED inherent capacitances, τ_r is $\tau_r = \left(\frac{2C_j}{\beta I_{Tx}} + \tau_m \right) \ln 9$. Here, $\beta = \frac{q}{2kT_s}$, $C_j = C_s + C_d$. Because the 3-dB frequency bandwidth of the Tx driving circuit is about $f_{Tx\_3dB} = \frac{1}{2\pi\tau_c} = \frac{1}{2\pi \left(\frac{2C_j}{\beta I_{Tx}} + \tau_m \right)} \approx \frac{0.35}{\tau_r}$ [46]. Therefore, with increasing I_{Tx}, decreasing C_j and τ_m, as well as decreasing temperature T_s, τ_r is decreased with faster energy transmission speed, and

f_{Tx_3dB} is improved. The τ_r depends heavily on the minority-carrier lifetime τ_m. In order to achieve LED high-frequency operation, C_j and τ_m needs to be reduced, and $I_{Tx}(t)$ needs to be used as high as practical [46], [58].

B. Rx Analyses

At Rx, PD can be divided into three types based on various operation modes: ordinary p-type/intrinsic/n-type (PIN) PDs, avalanche photodiodes (APDs), and single-photon avalanche diodes (SPADs). APDs are essentially PIN diodes operating at high reverse-bias voltages. Because of fast response time and little black electric current, APD and PIN PDs are the most widely used PD devices in VLC systems [47]. However, APD needs much higher reverse voltage than PIN PD, which is a big problem for many commercial embedded circuit implementations. Therefore, PIN PD is considered in this paper from a practical point of view.

To increase light intensity quality, an optical concentrator (OC) and an optical filter (OF) are manufactured before PD whose effect on light transmission should be considered. OF is used to avoid interference from information streams in other parts of the spectrum and avoids the negative effects of strong ambient light sources. The gain of OF is defined as $T_s(\psi)$ [15]. Any losses due to OC interface reflections or OF imperfections can be included in $T_s(\psi)$, which is set to be a constant in [15]. OC collects spectrum intensity into concentrated area to improve PD sensitivity. OC's gain is defined as $g(\psi) = (n^2)/(\sin^2(\psi_{FOV}))$, when $|\psi| \leq \Psi_{FOV}$ [48], n is internal refraction order, ψ is the incidence angle. When $|\psi| > \Psi_{FOV}$, $g(\psi) = 0$. The Ψ_{FOV} is determined by PD type. For semisphere PD, $\Psi_{FOV} \leq \pi/2$ usually. As FOV is reduced, $g(\psi)$ within the FOV is increased. If PD achieves $\Psi_{FOV} \approx \pi/2$, then $g(\psi) \approx n^2$ over entire FOV. If $\psi > \Psi_{FOV}$, Rx does not detect any light [15]. Effective light collection area of PD with OC and OF is $A_{Rx}^{eff}(\psi) = A_{Rx}T_s(\psi)g(\psi)\cos(\psi)$, when $|\psi| \leq \Psi_{FOV}$. When $\psi > \Psi_{FOV}$, $A_{Rx}^{eff}(\psi) = 0$.

PD vender always gives the relationship diagrams between wavelength λ and generated current/power, with unit of A/W. Define $Z(\lambda)$ to represent the PD circuit current response by radiant optical power, as shown in Figs. 3 (e) and (f) with blue dash-dot lines, which are from LSSPD-1.2 Lightsensing Ltd. [49] and 602PX First Sensor Ltd. [50] respectively. Luong [51] estimated the electrical signal at APD device output $I_{Rx}(t) = \bar{g}(t) \times Z(\lambda) \times P_{Rx}(t; \lambda)$. The PD average gain $\bar{g}(t)$ varies in accordance with the change of PD induced current. However, Luong just simply supposed $Z(\lambda) = 1$ when optical wavelength $\lambda = 1.55$ Î¼m with an InGaAs APD Rx, and set $\bar{g}(t)$ to be a constant which cannot reflect real PD's transmission characteristics. So more general calculations of the Rx response function need to be taken into account. Haas [45] stated that $Z(\lambda)$ response function is a constant calculated by integrating PD responses over the transmitted light signal spectrum. However, it has obvious deficiency because instantaneous values of both $Z(\lambda)$ and radiant optical power P_{Rx} are varying along wavelength λ. They cannot be simply considered as constant.

There are similar curve shapes for different PIN PD $Z(\lambda)$. Because the PD's response is basically a Gaussian distribution

form with center point migrated, the fitted 2nd order exponential function curves are with reasonable correctness to match the response curve, and make the model derivations easier, as plotted with red-solid lines in Figs. 3 (e) and (f).

$$Z(\lambda) = z\_a1 \cdot \exp\left(-\frac{\lambda - z\_b1}{z\_c1}\right)^2$$
$$+ z\_a2 \cdot \exp\left(-\frac{\lambda - z\_b2}{z\_c2}\right)^2. \quad (5)$$

Define $I_{Rx\_i}(t)$ as the Rx induced immediate photocurrent which is generated by the integral summary of intensity power covering all visible light wavelength bands. Combining (3), it has

$$I_{Rx}(t) = I_{Rx\_i}(t) \cdot \bar{g}(t) = \bar{g}(t)\int_\lambda Z(\lambda) \cdot P_{Rx}(t; \lambda)d\lambda$$

$$= \bar{g}(t)\int_\lambda Z(\lambda)H(t)P_{Tx}(t; \lambda)d\lambda$$

$$= \bar{g}(t)H(t)\int_\lambda Z(\lambda)P_{Tx}(t; \lambda)d\lambda$$

$$= \bar{g}(t)H(t) \cdot A \cdot P_{Tx\_M} \cdot I_{Tx}(t)\big[b_2 I_{Tx}(t) + b_1\big] \quad (6)$$

$$A = \int_\lambda Z(\lambda) \cdot P_{Tx}(t; \lambda)d\lambda \Big/ \int_\lambda P_{Tx}(t; \lambda)d\lambda. \quad (7)$$

Here, $\bar{g}(t)$ is related with PD generated current. The $I_{Rx}(t)$ varies with the $P_{Rx}(t; \lambda)$, containing both DC and AC component. It has been observed that the PD saturates when input optical power levels is high [52]. Two primary factors contribute to the PD's saturation: space-charge screening of the intrinsic region electric field [52]–[54] and thermal limits [55]. The thermal limits are determined by the PD's power dissipation characteristics. The space charge creates an electric field that redistributes the bias electric field. For sufficiently high-optical input power levels, the space-charge-induced electric field can be strong enough to collapse the bias electric field, which then results in PD photocurrent decreasing [54], [61]. Thus, $I_{Rx}(t)$ is no longer proportional to the Rx intensity power. The AC response current decreases at high average DC illumination levels due to a build-up of carriers in the depletion region, accompanied by a partial collapse of the depletion region electric field [54].

Define $\tau(t)$ is the PD photocurrent pulse duration varying with transmission process. The output current can be assumed to be linearly proportional to the input power until the saturation photocurrent is reached. Then, as given in [53] and [62], let $\bar{g}(t) = \tanh\left(\frac{k}{\sqrt{2\pi}} \cdot \frac{T}{\tau(t)}\right)$, k is a constant. The $\bar{g}(t)$ is a function of signal pulse duration and signal period, and $I_{Rx}(t)$ is not linearly proportional to $I_{Rx\_i}(t)$. The PD becomes saturated at large $I_{Rx\_i}(t)$, and there is a transient build up of the space-charge leading to higher saturated current as the τ decreases. The PD's saturation can severely affect the performance of VLC system performance [53], which is considered during VLC system evaluations.

C. Channel Analyses

Conventional Kahn's channel response model [15] was improved in [18], [45], [63], and [64]. Lee's model [18] expressed channel multi-reflection response time delay using

a $\delta(t - \frac{\sum d}{c})$ function. However, the elements of multi-reflection surface pieces were not taken into account. Haas's model [45] calculated the optical power without considering time delay and multi-Txs cases. To get more accurate channel calculations, the LoS/non-LoS reflections of various surfaces and propagation delay of non-LoS reflections should be considered. Non-LoS propagation is dominated by diffuse reflections where the optical power energy reflected from each surface element follows the Lambertian distribution. Then, the kth non-LoS propagation response is calculated recursively from the $(k-1)^{th}$ reflection as

$$h^k(t;T;R) = \sum_{l=1}^{N_l} \sum_{u=1}^{N_s} h_l^{k-1}(t;T_l;\varepsilon_u) \cdot h_l^0(t;\varepsilon_u;R). \quad (8)$$

Here, $h^k(t;T;R)$ is the LoS/non-LoS channel response function, N_l is the number of LEDs to represent multi-Txs, N_s is the number of sub-surfaces in the kth reflection bounce, and ε_u is the sub-surface area for multipath reflections. Multipath reflection coefficients for separate N_s pieces are all included. In the supposed $\{X,Y,Z\}$ indoor room, each reflection surface is divided into small elements of size ε_u m^2. Then, $N_s = 2\left(XY + YZ + XZ\right)/\varepsilon_u$ [64].

Channel response of LoS case is given as

$$h^0(t;\varepsilon_u;R) = \rho_u^0(\lambda) \cdot R_0(\phi) \cdot \frac{A_{Rx}^{eff}(\psi)}{d_0^2}$$

$$= \rho_u^0(\lambda)\frac{(m_{u,0}+1)A_{Rx}}{2\pi d_{u,0}^2} \cos^m(\phi_{u,0}) \cdot \cos(\psi_{u,0})$$

$$\cdot T_s(\psi_{u,0}) \cdot g(\psi_{u,0})\text{rect}\left(\frac{\psi_{u,0}}{\text{FOV}}\right)\delta\left(t - \frac{d_{u,0}}{c}\right). \quad (9)$$

Here, $\rho(\lambda)$ is element surface reflectivity coefficient which is specific to various surface material and wavelength. The smooth surface has a more directional emission pattern which can be modeled by adjusting the order m of the Lambertian radiation pattern. The majority of the reflective surfaces is not smooth and exhibits as a Lambertian radiation pattern with a half-angle $\Phi_{\frac{1}{2}}$. rect(x) is a function to indicate that only the light ray within the PD FOV can be detected [18]. When $|x| \le 1$, $rect(x) = 1$, else, $rect(x) = 0$.

Each reflection response is calculated by recursion way based on (8). The 1st bounce response $h^1(t;T;R)$ is calculated by summarizing all multiplication results of reflection piece responses of $h^0(t;\varepsilon_u;R)$, i.e., $h^1(t;T;R) = \sum_{l=1}^{N_l} \sum_{u=1}^{N_s} h_l^0(t;T_l;\varepsilon_u) \cdot h_l^0(t;\varepsilon_u;R)$. The 2nd bounce response $h^2(t;T;R)$ summarizes all multiplication results of reflection piece responses $h^1(t;T;\varepsilon_u)$ and $h^0(t;\varepsilon_u;R)$, i.e., $h^2(t;T;R) = \sum_{l=1}^{N_l} \sum_{u=1}^{N_s} h_l^1(t;T_l;\varepsilon_u) \cdot h_l^0(t;\varepsilon_u;R)$. The kth bounce $h^k(t;T;R)$ is calculated in the same way with all individual Tx and Rx surface elements, i.e.,

$$h^k(t;T;R)$$
$$= \sum_{l=1}^{N_l} \sum_{u=1}^{N_s} h_l^{k-1}(t;T_l;\varepsilon_u) \cdot h_l^0(t;\varepsilon_u;R)$$

$$= \sum_{l=1}^{N_l} \sum_{u=1}^{N_s} \left\{ \sum_{l'=1}^{N_l'} \sum_{u'=1}^{N_s'} \left\{ \cdots \left\{ \sum_{l^k=1}^{N_l^k} \sum_{u^k=1}^{N_s^k} \left[h_{l^k}^0(t;T_{l^k};\varepsilon_{u^k}^k) \right. \right. \right.$$
$$\left. \left. \left. \cdot h_{l^k}^0(t;\varepsilon_{u^k}^k;\varepsilon_{u^{k-1}}^{k-1}) \right] \right\} \cdots h_l^0(t;\varepsilon_{u'};\varepsilon_u) \right\} h_l^0(t;\varepsilon_u;R) \right\}$$

$$= \sum_{l=1}^{N_l} \sum_{u=1}^{N_s} \left\{ \sum_{l'=1}^{N_l'} \sum_{u'=1}^{N_s'} \left\{ \cdots \left\{ \sum_{l^k=1}^{N_l^k} \sum_{u^k=1}^{N_s^k} \left[h_{l^k}^0(t;T_{l^k};\varepsilon_{u^k}^k) \right. \right. \right.$$
$$\left. \left. \left. \cdot h_{l^k}^0(t;\varepsilon_{u^k}^k;\varepsilon_{u^{k-1}}^{k-1}) \cdots h_l^0(t;\varepsilon_{u'};\varepsilon_u) h_l^0(t;\varepsilon_u;R) \right] \right\} \cdots \right\} \right\}$$

$$= \sum_{l=1}^{N_l} \sum_{u=1}^{N_s} \left\{ \cdots \left\{ \sum_{l^k=1}^{N_l^k} \sum_{u^k=1}^{N_s^k} \left[\prod_{i=0}^{k} h_{l^i}^0(t;\varepsilon_{u^{i+1}}^{i+1};\varepsilon_{u^i}^i) \right] \right\} \cdots \right\}. \quad (10)$$

Here, $\varepsilon_{u^{k+1}}^{k+1} = T_{l^i}$ and $\varepsilon_{u^0}^0 = R_{l^i}$. After k bounces ($k \ge 1$), $P_{Rx}^k(t;\lambda) = P_{Tx}(\lambda)h^k(t;T;R)$. The optical power from the first N_r reflections is $P_{Rx}(t;\lambda) = \sum_{k=0}^{N_r} P_{Rx}^k(t;\lambda)$. Specifically, LoS optical power is calculated as

$$P_{Rx}^0(t;\lambda) = \sum_{l=1}^{N_l} P_{l,Tx}(\lambda) \cdot h^0(t;T;R)$$

$$= \sum_{l=1}^{N_l} \left[P_{l,Tx}(\lambda) \cdot \rho^0(\lambda) \cdot \frac{(m+1)A_{Rx}}{2\pi d_0^2} \cos^m \phi_0 \cos \psi_0 \right.$$
$$\left. \cdot T_s(\psi_0)g(\psi_0)\delta\left(t - \frac{d_0}{c}\right)\text{rect}\left(\frac{\psi_0}{\text{FOV}}\right) \right]. \quad (11)$$

The time delay for each LoS and non-LoS reflection path is different. They deeply affect the re-generated electric current in the PD. When non-LoS channel delays are comparable or greater than the symbol signal duration period T_p, they would be treated as noise for the next samples transmission. That causes inter-symbol interference (ISI) which is a critical factor for data reproduction. ISI becomes worse when the optical reflections number and distance increase [15]. ISI noise current is related not only with non-LoS multi-reflections, but also with T_p. Calculating the non-LoS channel multi-reflection timing delay is important for estimating electric current ISI noise. The kth bounce time delay reaching to the PD is $(\sum_{i=0}^{k} d_i)/c$. Here, d_i is calculated for each non-LoS reflection path, which is as quick as high-speed T_p in nanosecond level. If $(\sum_{i=0}^{k} d_i)/c > T_p$, the multi-reflection non-LoS electric current becomes noise current for the following sample transmissions.

D. Current Energy Transferring Calculation Model

Based on (10), considering multi-reflection time delay and wavelength λ, Rx optical power $P_{Rx}(t;\lambda)$ of the kth reflections can be calculated by

$$P_{Rx}^k(t;\lambda) = P_{Tx}(\lambda) \cdot h^k(t;T;R) = \sum_{l=1}^{N_l} \sum_{u=1}^{N_s}$$

$$\times \left\{ \cdots \left\{ \sum_{l^k=1}^{N_l^k} \sum_{u^k=1}^{N_s^k} \left[\prod_{i=0}^{k} P_{l,Tx}(\lambda) \cdot h_{l^i}^0(t;\varepsilon_{u^{i+1}}^{i+1};\varepsilon_{u^i}^i) \right] \right\} \cdots \right\}. \quad (12)$$

The total optical power from the first N_r reflections is

$$P_{Rx}(t;\lambda) = \sum_{k=0}^{N_r} P_{Rx}^k(t;\lambda)$$

$$= \sum_{k=0}^{N_r}\sum_{l=1}^{N_l}\sum_{u=1}^{N_s}\left\{\cdots\left\{\sum_{l^k=1}^{N_l^k}\sum_{u^k=1}^{N_s^k}\left[\prod_{i=0}^{k} P_{l,Tx}(\lambda)\right.\right.\right.$$

$$\left.\left.\left.\cdot h_{l^k}^0\left(t;\varepsilon_{u^{i+1}}^{i+1};\varepsilon_{u^i}^i\right)\right]\right\}\cdots\right\}$$

$$= \sum_{k=0}^{N_r}\sum_{l=1}^{N_l}\sum_{u=1}^{N_s}\left\{\cdots\left\{\sum_{l^k=1}^{N_l^k}\sum_{u^k=1}^{N_s^k}\left[\prod_{i=0}^{k} P_{l,Tx}(\lambda)\right.\right.\right.$$

$$\cdot\rho^i(\lambda)\frac{(m+1)\varepsilon_{u^i}^i}{2\pi d_i^2}\cos\psi_i$$

$$\cdot\cos^m\phi_i T_s(\psi_i)g(\psi_i)\delta\left(t-\frac{\sum_{j=0}^k d_j}{c}\right)$$

$$\left.\left.\left.\cdot\text{rect}\left(\frac{\psi_i}{\text{FOV}}\right)\right]\right\}\cdots\right\}. \tag{13}$$

Here, $T_s(\psi)$ and $g(\psi)$ are related with ψ and m is calculated by $\Phi_{\frac{1}{2}}$. When relative position between the Tx and Rx is changed, response power is then changed with ψ, ϕ and d_0.

LoS case is useful for clarifying the basic relationship between VLC hardware current energy and optical power. Based on (11), $P_{Rx}^0(t)$ covers all visible light wavelength range, i.e.,

$$P_{Rx}^0(t) = \int_\lambda \sum_{l=1}^{N_l} P_{l,Rx}(t;\lambda)d\lambda$$

$$= \int_\lambda \sum_{l=1}^{N_l}\left[P_{l,Tx}(t;\lambda)\cdot\rho^0(\lambda)\frac{(m+1)A_{Rx}}{2\pi d_0^2}\right.$$

$$\cot\cos^m\phi_0\cos\psi_0 T_s(\psi_0)$$

$$\left.\cdot g(\psi_0)\delta\left(t-\frac{d_0}{c}\right)\text{rect}\left(\frac{\psi_0}{\text{FOV}}\right)d\lambda\right]$$

$$= \sum_{l=1}^{N_l}\left[\frac{(m+1)A_{Rx}}{2\pi d_0^2}\cos^m\phi_0\right.$$

$$\cdot\cos\psi_0 T_s(\psi_0)g(\psi_0)\delta\left(t-\frac{d_0}{c}\right)$$

$$\left.\cdot\text{rect}\left(\frac{\psi_0}{\text{FOV}}\right)\cdot\int_\lambda P_{l,Tx}(\lambda)\cdot\rho^0(\lambda)d\lambda\right]. \tag{14}$$

If let $\rho(\lambda)$ be a constant ρ, based on (3) and (14), there has

$$P_{Rx}^0(t) = \sum_{l=1}^{N_l}\left[\rho\cdot\frac{(m+1)A_{Rx}}{2\pi d_0^2}\cos^m(\phi_0)\cos\psi_0 T_s(\psi_0)g(\psi_0)\right.$$

$$\left.\cdot\delta\left(t-\frac{d_0}{c}\right)\text{rect}\left(\frac{\psi_0}{\text{FOV}}\right)P_{Tx\_M}I_{Tx}\left(b_1+b_2 I_{Tx}\right)\right]. \tag{15}$$

From (14) and (15), received optical power can be directly calculated from Tx optical power or Tx circuit current. These build up the basic calculation model between Tx and Rx current energy. Based on (6) and (14), $I_{Rx}^0(t)$ can be further deduced as

$$I_{Rx}^0(t) = \bar{g}(t)\int_\lambda Z(\lambda)\cdot\sum_{l=1}^{N_l} P_{l,Rx}^0(t;\lambda)d\lambda$$

$$= \bar{g}(t)\sum_{l=1}^{N_l}\int_\lambda Z(\lambda)\cdot P_{l,Rx}^0(t;\lambda)d\lambda$$

$$= \bar{g}(t)\sum_{l=1}^{N_l}\left\{\left[\rho\cdot\frac{(m+1)A_{Rx}}{2\pi d_{l,0}^2}\right.\right.$$

$$\cdot\cos^m(\phi_{l,0})\cos(\psi_{l,0})T_s(\psi_{l,0})g(\psi_{l,0})$$

$$\left.\cdot\delta\left(t-\frac{d_{l,0}}{c}\right)\text{rect}\left(\frac{\psi_{l,0}}{\text{FOV}}\right)\right]$$

$$\left.\cdot\left[\int_\lambda Z(\lambda)\cdot P_{l,Tx}(\lambda)d\lambda\right]\right\}. \tag{16}$$

At time $t=\frac{d_0}{c}$ and with $\frac{\psi_0}{\text{FOV}}\leq 1$, the induced current value in Rx hardware circuit is

$$I_{Rx}^0(t)\Big|_{t=\frac{d_0}{c}}^{\left|\frac{\psi_0}{\text{FOV}}\right|\leq 1}$$

$$= \bar{g}(t)\sum_{l=1}^{N_l}\left\{\rho\cdot\frac{(m+1)A_{Rx}}{2\pi d_{l,0}^2}\cos^m(\phi_{l,0})\cos(\psi_{l,0})\right.$$

$$\left.\cdot T_s(\psi_{l,0})g(\psi_{l,0})\left[\int_\lambda Z(\lambda)\cdot P_{l,Tx}(\lambda)d\lambda\right]\right\}. \tag{17}$$

And here,

$$\int_\lambda Z(\lambda)\cdot P_{Tx}(\lambda)d\lambda = \int_\lambda\left[z\_a1\cdot\exp\left(-\frac{\lambda-z\_b1}{z\_c1}\right)^2\right.$$

$$\left.+z\_a2\cdot\exp\left(-\frac{\lambda-z\_b2}{z\_c2}\right)^2\right]$$

$$\cdot\left[p\_a1\cdot\exp\left(-\frac{\lambda-p\_b1}{p\_c1}\right)^2\right.$$

$$\left.+p\_a2\cdot\exp\left(-\frac{\lambda-p\_b2}{p\_c2}\right)^2\right]d\lambda. \tag{18}$$

Non-LoS multipath reflection current value is calculated by inserting (12) into (6), i.e.,

$$I_{Rx}^k(t) = \bar{g}(t)\int_\lambda Z(\lambda)\cdot P_{Rx}^k(t;\lambda)d\lambda$$

$$= \bar{g}(t)\int_\lambda Z(\lambda)\cdot\left\{\sum_{l=1}^{N_l}\sum_{u=1}^{N_s}\left\{\cdots\left\{\sum_{l^k=1}^{N_l^k}\sum_{u^k=1}^{N_s^k}\right.\right.\right.$$

$$\left.\left.\left.\cdot\left[\prod_{i=0}^{k} P_{l,Tx}(\lambda)\cdot h_{li}^0(t;\varepsilon_{u^{i+1}}^{i+1};\varepsilon_{u^i}^i)\right]\right\}\cdots\right\}\right\}d\lambda$$

$$= \bar{g}(t)\sum_{l=1}^{N_l}\sum_{u=1}^{N_s}\left\{\cdots\left\{\sum_{l^k=1}^{N_l^k}\sum_{u^k=1}^{N_s^k}\left\{\prod_{i=0}^{k}\right.\right.\right.$$

$$\left[\frac{(m+1)\varepsilon_{u^i}^i}{2\pi d_i^2}\cos^m\phi_i\cos\psi_i\cdot\right.$$

$$\left.T_s(\psi_i)g(\psi_i)\delta\left(t-\frac{\sum_{j=0}^k d_j}{c}\right)\text{rect}\left(\frac{\psi_i}{\text{FOV}}\right)\right]\cdot$$

$$\left.\left.\left.\left[\int_\lambda Z(\lambda)P_{l,Tx}(\lambda)\cdot\left(\prod_{i=0}^k \rho^i(\lambda)\right)d\lambda\right]\right\}\right\}\cdots\right\}. \tag{19}$$

Then, at time $t = \dfrac{\sum_{j=0}^{k} d_j}{c}$ and with each $\dfrac{\psi_i}{\text{FOV}} \leq 1$, the induced k^{th} hardware current at Rx is

$$
I_{Rx}^{k}(t)\Big|_{t=\frac{\sum_{j=0}^{k} d_j}{c}}^{\frac{\psi_i}{\text{FOV}} \leq 1}
$$

$$
= \bar{g}(t) \sum_{l=1}^{N_l} \sum_{u=1}^{N_s} \left\{ \cdots \left\{ \sum_{l^k=1}^{N_l^k} \sum_{u^k=1}^{N_s^k} \left\{ \prod_{i=0}^{k} \right. \right. \right.
$$

$$
\cdot \frac{(m+1)\varepsilon_{u^i}^{i}}{2\pi d_i^2} \cos^m \phi_i \cdot \cos \psi_i T_s(\psi_i) g(\psi_i) \Big]
$$

$$
\left. \left. \left. \cdot \left[\int_{\lambda} Z(\lambda) \cdot P_{l,Tx}(\lambda) \cdot \left(\prod_{i=0}^{k} \rho^i(\lambda) \right) d\lambda \right] \right\} \right\} \cdots \right\}.
$$

(20)

Define parameters $L_{l,u,i}$, $\mathfrak{P}$, and $W(l,\lambda)$ as

$$
L_{l,u,k} = \prod_{i=0}^{k} \frac{(m+1)\varepsilon_{u^i}^{i}}{2\pi d_{l,u,i}^2} \cos(\psi_{l,u,i})
$$

$$
\cdot \cos^m(\phi_{l,u,i}) T_s(\psi_{l,u,i}) g(\psi_{l,u,i}) \delta
$$

$$
\cdot \left(t - \frac{\sum_{j=0}^{k} d_{l,u,j}}{c} \right) \text{rect}\left(\frac{\psi_{l,u,i}}{\text{FOV}} \right),
$$

$$
\mathfrak{P} = \prod_{i=0}^{k} \rho_{l,u}^{i}(\lambda), \quad W(l,\lambda) = Z(\lambda) \cdot P_{l,Tx}(\lambda) \cdot \mathfrak{P},
$$

$$
\int_{\lambda} W(l,\lambda) \cdot d\lambda = A \cdot P_{Tx} \cdot I_{Tx}\left(t - \frac{\sum_{j=0}^{k} d_j}{c} \right)
$$

$$
\cdot \left[b_2 I_{Tx} + b_1 \left(t - \frac{\sum_{j=0}^{k} d_j}{c} \right) \right].
$$

(21)

In practice, $\mathfrak{P}$ can be a constant. The induced current $I_{Rx}(t)$ with both LoS and non-LoS optical power from the first N_r reflections is obtained by (6) and (13), i.e.,

$$
I_{Rx}(t) = \bar{g}(t) \int_{\lambda} Z(\lambda) \cdot P_{Rx}(t;\lambda) d\lambda
$$

$$
= \bar{g}(t) \int_{\lambda} Z(\lambda) \cdot \left\{ \sum_{k=0}^{N_r} \sum_{l=1}^{N_l} \sum_{u=1}^{N_s} \left\{ \cdots \left\{ \sum_{l^k=1}^{N_l^k} \sum_{u^k=1}^{N_s^k} \right. \right. \right.
$$

$$
\left[\prod_{i=0}^{k} P_{l,Tx}(\lambda) \rho^i(\lambda) \frac{(m+1)\varepsilon_{u^i}^{i}}{2\pi d_i^2} \cos \psi_i \cos^m \phi_i T_s(\psi_i) \right.
$$

$$
\left. \left. \left. \cdot g(\psi_i) \delta\left(t - \frac{\sum_{j=0}^{k} d_j}{c} \right) \text{rect}\left(\frac{\psi_i}{\text{FOV}} \right) \right] \right\} \cdots \right\} \right\} d\lambda
$$

$$
= \bar{g}(t) \sum_{k=0}^{N_r} \sum_{l=1}^{N_l} \sum_{u=1}^{N_s} \left\{ \cdots \left\{ \sum_{l^k=1}^{N_l^k} \sum_{u^k=1}^{N_s^k} \right. \right.
$$

$$
\left\{ \left[\prod_{i=0}^{k} \frac{(m+1)\varepsilon_{u^i}^{i}}{2\pi d_i^2} \cos \psi_i \cos^m \phi_i \right. \right.
$$

$$
\cdot T_s(\psi_i) g(\psi_i) \delta\left(t - \frac{\sum_{j=0}^{k} d_j}{c} \right) \text{rect}\left(\frac{\psi_i}{\text{FOV}} \right) \Big] \cdot
$$

$$
\left. \left. \left. \left[\int_{\lambda} Z(\lambda) \cdot P_{l,Tx}(\lambda) \cdot \left(\prod_{i=0}^{k} \rho^i(\lambda) \right) d\lambda \right] \right\} \right\} \cdots \right\}
$$

$$
= \bar{g}(t) \sum_{k=0}^{N_r} \sum_{l=1}^{N_l} \sum_{u=1}^{N_s} \left\{ \cdots \left\{ \sum_{l^k=1}^{N_l^k} \sum_{u^k=1}^{N_s^k} \left\{ L_{l,u,k} \right. \right. \right.
$$

$$
\cdot \left(\int_{\lambda} W(l,\lambda) \cdot d\lambda \right) \Big\} \Big\} \cdots \Big\}
$$

$$
= \tanh\left(\frac{k}{\sqrt{2\pi}} \cdot \frac{T}{\tau(t)} \right) \cdot \sum_{k=0}^{N_r} \sum_{l=1}^{N_l} \sum_{u=1}^{N_s} \left\{ \cdots \left\{ \sum_{l^k=1}^{N_l^k} \sum_{u^k=1}^{N_s^k} \right. \right.
$$

$$
\left\{ L_{l,u,k} \left[A \cdot P_{Tx\_M} \cdot I_{Tx} \cdot \left(t - \frac{\sum_{j=0}^{k} d_j}{c} \right) \right. \right.
$$

$$
\left. \left. \left. \left. \cdot \left[b_1 + b_2 I_{Tx}\left(t - \frac{\sum_{j=0}^{k} d_j}{c} \right) \right] \right] \right\} \right\} \cdots \right\}.
$$

(22)

The Rx response changes with the Tx current energy. The maximum and minimum Rx optical power values determine the critical VLC system settings and evaluations. Let us define the maximum and minimum Rx optical powers as P_{Rx_H} and P_{Rx_L} respectively. The corresponding induced maximum and minimum currents are I_{Rx_H} and I_{Rx_L}. Note that I_{Rx_L} is the minimum current keeping Rx hardware circuit working, while I_{Rx_H} is limited by PD's saturation characteristic. So, to keep the VLC system working with high-performance and energy transferring efficiency, the maximum and minimum Tx current energy should be carefully calculated based on the I_{Rx_H} and I_{Rx_L} values.

As given in (16), (19), and (22), the derived current energy transferring calculation model (CETCM) describes the complicated function between current energy and optical parameters. Several useful items are indicated by the CETCM:

1) Only focusing on the optical power is far from sufficient for clarifying VLC system behaviors. CETCM can reflect the basic system working mechanisms which are important for fully understanding the hardware design of VLC systems.

2) It is critical and valuable to calculated VLC system gain based on circuit current energy. The gain between $I_{Tx}(t)$ and $I_{Rx}(t)$ indicates the energy transfer efficiency-ratio between the Tx and Rx. The peak-value of $I_{Rx}(t)$ can be calculated based on CETCM, and can help to select the matched optical devices for both the Tx and Rx.

3) When $I_{Tx}(t)$ is higher, $I_{Rx}(t)$ is not linearly induced because of PD saturation responses. So to enlarge $I_{Rx}(t)$, simply increase $I_{Tx}(t)$ cannot get ideal result. The T_p, signal duration time, and the distance between Tx and Rx are also related to non-linear $I_{Rx}(t)$ responses.

4) When the relative position between the Tx and Rx is fixed, increasing A_{Rx}, enlarging FOV, or increasing supply current can directly increase PD induced current. That has many benefits for VLC system, such as improving signal-to-noise ratio and making filter design easier for Rx signals regeneration.

5) When A_{Rx} is fixed, if we change the relative position of the Tx and Rx, $I_{Rx}(t)$ will change in approximate square function way. d must have specific limitation to guarantee the Rx circuit working status.

6) When d and A_{Rx} are fixed, change the incident angle ϕ and ψ can change the induced current non-linearly. When both $\psi = 0°$ and $\phi = 0°$, $I_{Rx}(t)$ reaches to the maximum value. If turning PD or LED devices to other orientations, $I_{Rx}(t)$ will decrease accordingly.

III. CURRENT ENERGY TRANSFERRING PARAMETERS AND EVALUATIONS

A. Peak Current Energy Response

Let us suppose that the frequency of transmitted sample signal is f_s, corresponding period is $T_p = 1/f_s$. The $I_{Rx}(t)$ $(0 \leq t \leq T)$ is re-generated by both LoS/non-LoS optical power. Peak current energy response (PCER) parameter is defined as the peak Rx electric current response along with visible light wavelength. With (1) and (5), we can get $PCER(\lambda)$ as

$$
\begin{aligned}
PCER(\lambda) &= \max \left[Z(\lambda) \cdot P_{Tx}(\lambda) \right] \\
&= \max \left\{ \left[z\_a1 \cdot \exp \left(-\frac{\lambda - z\_b1}{z\_c1} \right)^2 \right. \right. \\
&\quad + z\_a2 \cdot \exp \left(-\frac{\lambda - z\_b2}{z\_c2} \right)^2 \right] \cdot \\
&\quad \left[p\_a1 \cdot \exp \left(-\frac{\lambda - p\_b1}{p\_c1} \right)^2 + p\_a2 \right. \\
&\quad \left. \left. \cdot \exp \left(-\frac{\lambda - p\_b2}{p\_c2} \right)^2 \right] \right\}.
\end{aligned}
$$
(23)

Because $PCER(\lambda)$ presents the most sensitive wavelength value which has the peak electric current response in Rx hardware circuit. So, $PCER(\lambda)$ is used to direct the selection of the suitable LED and PD devices to optimize Rx responses of a VLC system.

B. Current Energy Gain

Circuit current value determines circuit driving capability in VLC system implementation. While the current energy transferring efficiency determines the quality of VLC system implementations. The value ratio between the Tx and Rx hardware circuit current is defined as the current energy gain (CEG), i.e.,

$$
\begin{aligned}
\mathrm{CEG} &= \frac{I_{Rx}(t)}{I_{Tx}(t)} \\
&= \frac{\bar{g}(t) \sum\limits_{k=0}^{N_r} \sum\limits_{l=1}^{N_l} \sum\limits_{u=1}^{N_s} \left\{ \cdots \left\{ \sum\limits_{l^k=1}^{N_l^k} \sum\limits_{u^k=1}^{N_s^k} \left\{ L_{l,u,k} \int_\lambda W(l,\lambda) \cdot d\lambda \right\} \right\} \cdots \right\}}{\sum\limits_{l=1}^{N_l} \left(\frac{-b_1 \pm \sqrt{b_1^2 + \frac{4b_2}{P_{Tx\_M}} \cdot \int_\lambda P_{Tx}(\lambda) d\lambda}}{2b_2} \right)}.
\end{aligned}
$$
(24)

The CEG is different from the system power gain presented by Haas [45] or Lee [18]. It reflects the current energy transferring efficiency. The CEG is related with λ, $Z(\lambda)$, $\bar{g}(t)$, reflection path distance/angle, and $P_{Tx}(\lambda)$. When $I_{Tx}(t)$ is a specific value, to keep VLC system working, the channel and device parameters should be selected to fulfill $\mathrm{CEG} \geq I_{Rx\_L}/I_{Tx}(t)$. On the other hand, if the VLC system channel and devices are fixed, the minimum supply current is required to be $I_{Tx\_L} \geq I_{Rx\_L}/\mathrm{CEG}$.

C. Threshold of Optical Power Transferring Distance

Distance parameter has very important influence on VLC system responses. It has already been proved by Kahn and Barry [15] and Lee *et al.* [18] that LoS optical power occupies the main radiant optical power of transmission. Then, there exists the maximum and minimum distance threshold to maintain Rx working correctly. Because the optical power of non-LoS has limit impact on the transferring distance threshold. So the LoS optical power transferring distance threshold $\mathrm{OPTD_{TH}}$ is the main factor to evaluate VLC system transmission distance. Based on (16), when optical power transmitted by each LED Tx is the same, $\mathrm{OPTD_{TH}}$ is

$$
\begin{aligned}
\mathrm{OPTD_{TH}} &= \sqrt{\frac{N_l \cdot \mathfrak{D} \cdot \left[P_{Tx\_M} \int_\lambda Z(\lambda) P_{l,Tx}(\lambda) d\lambda \right]}{I_{Rx}(t)}}, \\
\mathfrak{D} &= \bar{g}(t) \cdot \frac{(m+1)A_{Rx}}{2\pi} \cos\psi_0 \cos^m\phi_0 T_s(\psi_0) g(\psi_0) \\
&\quad \cdot \delta\left(t - \frac{d_0}{c} \right) \mathrm{rect}\left(\frac{\psi_0}{\mathrm{FOV}} \right).
\end{aligned}
$$
(25)

So, $\mathrm{OPTD_{TH}}$ is under the control of $I_{Tx}(t)$, and $\mathrm{OPTD_{TH}} \propto \sqrt{\frac{\int_\lambda Z(\lambda) P_{l,Tx}(\lambda) d\lambda}{I_{Rx}(t)}}$. When the I_{Tx_L} drives VLC system, the minimum induced Rx current I_{Rx_L} determines the low-end threshold of transferring distance $OPTD_{TH\_L}$. Because of PD saturation characteristic, the transferring distance has high-end threshold value $OPTD_{TH\_H}$. Therefore, in VLC system, if $d_0 \geq \mathrm{OPTD_{TH\_L}}$ or $d_0 \leq \mathrm{OPTD_{TH\_H}}$, there are no responses at the Rx circuit, and the transmitted data would be lost. The $\mathrm{OPTD_{TH}}$ is the communication distance threshold limitation in the designed VLC system which is important for system evaluations.

D. Current Signal-to-Noise Ratio

Noise current $I_{Rx\_n}(t)$ is also an important factor for VLC system. There are three major sources of noise in indoor VLC system [2]. One is ambient light noise due to solar radiation or other illumination sources such as incandescent and fluorescent lamps. It is a DC interference which can be mitigated by an electrical high pass filter at the Rx. The other is shot noise induced by the PD generated current. It can be treated as a stationary Gaussian random process [57]. The last one is electrical pre-amplifier noise (also known as thermal noise) of the PD. The dark current and flicker noise current can be ignored [51] [59].

Besides the three sources, the non-LoS multipath reflections could also generate noise current. The LoS radiant optical power induces electric current at time $\mathrm{d_{LoS}}/c$. Electric current generated by non-LoS power is in succession with time delay $\frac{\sum_{i=0}^{k} d_i}{c}$. If $\frac{\sum_{i=0}^{k} d_i}{c} \leq \left(\frac{1}{f_s} + \frac{\mathrm{d_{LoS}}}{c} \right)$, the non-LoS power generates the correct current signal. Otherwise, it would be

added to the next sample's LoS intensity power, and become the next samples noise current. The situation would become more serious when samples are transmitted in high-frequency. Define $I_{Rx\_r}(t)$ is the noise current generated by non-LoS multi-path reflections power whose path distance is longer than $c/f_s + \mathrm{d}_{\mathrm{LoS}}$.

Therefore, noise current $I_{Rx\_n}(t)$ mainly includes non-LoS reflection noise current $I_{Rx\_r}(t)$, shot noise current $I_{Rx\_s}(t) = \bar{g}(t)\sqrt{2\ I_{Rx}(t)B_n}$ and thermal noise current $I_{Rx\_t}(t) = \sqrt{4kT_eB_n/R_l}$ [58] [60]. Here, Boltzmann constant $k = 1.38 \times 10^{-23} J/K$. Te is the Rx equivalent noise temperature in Kelvin degree, R_l is the PD's load equivalent resistance, B_n is the the effective noise bandwidth, respectively. B_n can be equal to half of system bit rate R_b [59]. Since $I_{Rx\_r}(t)$, $I_{Rx\_s}(t)$ and $I_{Rx\_t}(t)$ are independent Gaussian random processes, the total variance of noise can be obtained simply by adding them together, $I_{Rx\_n}(t) = I_{Rx\_r}(t) + I_{Rx\_s}(t) + I_{Rx\_t}(t)$. Then

$$
\begin{aligned}
\mathrm{C} - \mathrm{SNR}(t) &= \frac{I_{Rx}(t) - I_{Rx\_r}(t)}{I_{Rx\_n}(t)} \\
&= \left\{ \sum_{k=0}^{N_r}\sum_{l=1}^{N_l}\sum_{u=1}^{N_s}\left\{ \cdots \left\{ \sum_{l^k=1}^{N_l^k}\sum_{u^k=1}^{N_s^k}\left\{ L_{l,u,k} \right.\right.\right.\right. \\
&\left.\left.\left.\left. \cdot \int_{\lambda}W(l,\lambda)d\lambda \right\} \cdots \right\}\right\} - \\
&\sum_{k=0}^{N_r}\sum_{l=1}^{N_l}\sum_{u=1}^{N_s}\left\{ \cdots \left\{ \sum_{l^k=1}^{N_l^k}\sum_{u^k=1}^{N_s^k}\bar{L} \right\} \cdots \right\}\right\} \Bigg/ \\
&\left\{ \sum_{k=0}^{N_r}\sum_{l=1}^{N_l}\sum_{u=1}^{N_s}\left\{ \cdots \left\{ \sum_{l^k=1}^{N_l^k}\sum_{u^k=1}^{N_s^k}\bar{L} \right\} \cdots \right\}\right. \\
&\left. + I_{Rx\_s}(t) + I_{Rx\_t}(t) \right\}.
\end{aligned} \tag{26}
$$

Here, $\bar{L} = L_{l,u,k}\Big|_{\sum_{i=0}^{k}d_i \geq (\frac{c}{f_s}+d_{LoS})} \cdot \int_{\lambda}W(l,\lambda)d\lambda$. C-SNR reflects the basic VLC circuit characteristics. I_{Rx_H} and I_{Rx_L} cause different C-SNR value. If $I_{Rx\_r}(t)$ is high compared to signal current, samples re-generation mistakes and BER would be increased. So, C-SNR indicates the quality of VLC system design. If C-SNR is low, the VLC system would be suffered from BER and be hard for high-frequency communications.

Based on the four defined parameters, which are $PCER(\lambda)$, current energy gain CEG, threshold of optical power transferring distance $\mathrm{OPTD}_{\mathrm{TH}}$, and C-SNR, the designed VLC system characteristics can be calculated accordingly. Together with CETCM, system bottle-neck and optimization methods can be further analyzed and evaluated.

IV. EXPERIMENTS AND SIMULATIONS

Two typical WLED response diagrams are given in Figs. 3 (a) to (d). Corresponding coefficients b_1 and b_2 in $P_{Tx}(I_{Tx})$ are $b_1 = 3.0$, $b_2 = -0.6$ for Nichia NCSWE17A device, and $b_1 = 2.7$, $b_2 = -0.83$ for CREE C513A device. The $P_{Tx}(\lambda)$ co-efficients are listed in Table II. The $Z(\lambda)$ is calculated by (5), with unit of A/Watt. Two typical PD $Z(\lambda)$

TABLE II
WLED OPTICAL POWER RESPONSE

LED type	a_1	b_1	c_1	a_2	b_2	c_2
Nichia NCSWE17A	0.94	445	13	0.6	570	81
CREE C513A	0.88	454	15.7	0.49	560	88

TABLE III
PD CURRENT/POWER RESPONSE

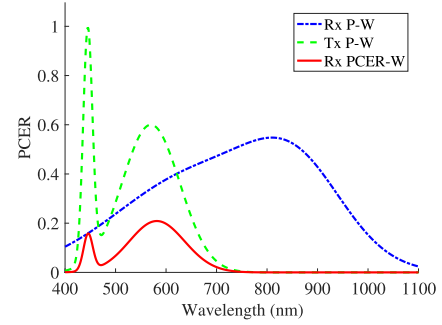| PD type	a_1	b_1	c_1	a_2	b_2	c_2
lightsensing	0.3104	858.7	134.2	0.4036	667.8	230.3
602px	0.3183	955.7	119.1	0.4833	726.4	324.3

Fig. 4. The peak current energy response $PCER(\lambda)$.

function coefficients are listed in Table III. The Nichia NC-SWE17A LED device and Lightsensing PIN PD device are used in this paper. Based on the published parameters, $A_{Rx} = 1.2 \times 1.2$ mm^2, $\Phi_{\frac{1}{2}} = \frac{\pi}{4}$, $\Phi = \frac{\pi}{2}$, $\Psi_{\mathrm{FOV}} = \frac{7\pi}{9}$, refraction order $n = 1$, and $m = \dfrac{-\ln(2)}{\ln\left(\cos\left(\Phi_{\frac{1}{2}}\right)\right)} = \dfrac{-\ln(2)}{\ln\left(\cos\left(\frac{\pi}{4}\right)\right)} = 1$, $g(\phi) = n^2 = 1$, and $T_s(\phi) = 1$.

Assume that the room size $X = 5$ m, $Y = 5$ m, $Z = 3$ m, the Rx is on a table with $H = 0.85$ m height, $N_r = 1$, $N_l = 4$, and $\varepsilon_u = (0.1 \times 0.1)$ cm^2, and $N_s = 4400$. Four Txs are fitted on the room ceiling, whose positions are given as $(X/4, Y/4, Z)$, $(3X/4, Y/4, Z)$, $(3X/4, 3Y/4, Z)$, and $(X/4, 3Y/4, Z)$. Rx positions are in the space from $(0, 0, H)$ to (X, Y, H). Wavelength range is $\lambda_L = 400$ nm to $\lambda_H = 800$ nm as given by NCSWE17A [39].

To evaluate response differences with various circuit current and position parameters, we classify static response and dynamic response. Static response means that $I_{Tx}(t)$ is a constant. Here, set $I_{Tx}(t) = 500$ mA. Dynamic response means that $I_{Tx}(t)$ changes within a range, such as from 200 mA to 500 mA. Based on (23), the $PCER(\lambda)$ is calculated, as shown in Fig. 4.

Based on (16) and (19), static LoS response $I_{Rx}^0(t)$ and one reflection response summary $I_{Rx}^1(t)$ are shown in Figs. 5 (a) and (b) respectively, with the same unit as $I_{Tx}(t)$. We can see that LoS component carries most of transmitting energy.

Assume that one Tx is at $(X/4, Y/4, Z)$. Static current response at Rx positions (X, Y, H), $(X/2, Y/2, H)$ and $(X/4, Y/4, H)$ are shown in Fig.6. The vertical orientation faced Tx/Rx position has the largest electric current
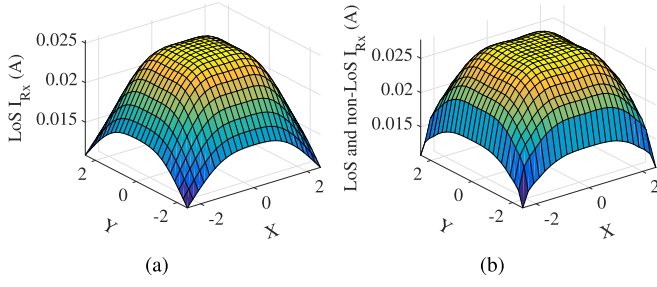
Fig. 5. (a) is the static LoS responses $I_{Rx}^0(t)$ and (b) is one reflection current response $I_{Rx}^1(t)$.
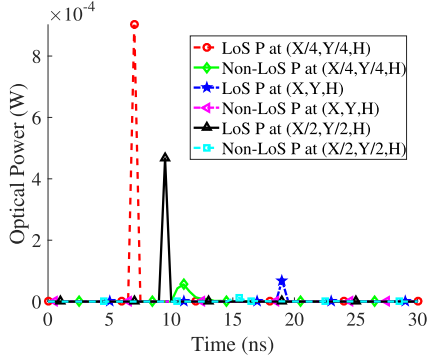

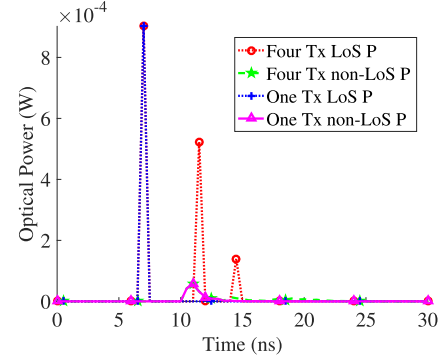Fig. 6. Different Rx optical power responses with one Tx at $(X/4, Y/4, Z)$.

Fig. 7. Rx optical power responses at $(X/4, Y/4, H)$ with one Tx at $(X/4, Y/4, Z)$ and four Txs.

Fig. 8. The Rx optical power responses at $(1, 1, H)$ with one Tx at $(X/4, Y/4, Z)$ and four Txs.

response. While the amplitude of LoS response at (X, Y, H) is even smaller than the non-LoS response amplitude at $(X/4, Y/4, H)$. So, LoS response has small effect for the non-rectangular Tx/Rx position. At (X, Y, H) Rx position, the LoS response is so small that even can be ignored.

If the Rx is at position $(X/4, Y/4, H)$, the different LoS distances and response time delays are shown in Fig. 7. Peak current is triggered by LoS optical power. The maximum Rx response occurs at the direct facing position to Tx, where the induced optical power is almost twice compared with the summary optical power from other three Tx positions. The time delay between the 2nd peak of LoS response and the non-LoS response at $(X/4, Y/4, H)$ is similar. The delay time between the 1st peak and the 2nd peak is about 10 ns, which is already very close to the signal sample period T_p with 100 MHz clock frequency. Considering the LoS and non-LoS optical power responses from other Txs, the induced optical power overlap would cause serious ISI problems at the Rxs. Fig. 8 shows optical power response at $(1, 1, H)$ which is the room corner position. Its LoS optical power occupies the main energy components. Non-LoS optical power is too small to be ignored because of the severe optical power transmitting fading.

The dynamic current responses with one Tx at $(X/4, Y/4, Z)$ are shown in Fig. 9 (a), four Txs are shown in Fig. 9 (b), with $I_{Tx}(t)$ changed from 200 mA to 500 mA. When $I_{Tx}(t)$ increases linearly, the $I_{Rx}(t)$ increases non-linearly. Larger $I_{Tx}(t)$ has higher current energy transfer efficiency when PD is not in saturation state.

Dynamic gain CEG with one or four Txs are calculated by (24). Fig. 9 (c) shows the CEG with one Tx at $(X/4, Y/4, Z)$. Fig. 9 (d) shows four Txs case. In one Tx

case, total CEG is almost 1.3 times of LoS CEG because of the Rx non-LoS optical power components. In four Txs case, CEG has about 50% increment compared with one Tx case. That aligns with the phenomenon shown in Fig. 7. The CEG increases non-linearly with $I_{Tx}(t)$. When the $I_{Tx}(t)$ is in a low level, increasing $I_{Tx}(t)$ is an efficient way to improve the efficiency of system energy transferring. However, because of the PD saturation characteristics, when $I_{Tx}(t)$ is increased to a specific high level, the $I_{Rx}(t)$ would not increase accordingly.

The VLC system has generally high energy loss. In the four Txs case, there are more than 95% energy loss because of transmission and energy conversion. Therefore, to design high-performance VLC system, the $I_{Tx}(t)$ must be high enough to make sure that the Rx optical power could trigger Rx hardware circuit working.

Supposing $I_{Rx\_L} = 10$ mA, OPTD_{TH} is calculated based on (25), as shown in Figs. 9 (e) and (f) respectively. $I_{Tx}(t)$ is changed from 200 mA to 500 mA. Optical power transmission distance can reach to about 1.1 m in one Tx case and 1.5m in four Txs case. That is an important directive parameter for VLC system design. If the required transmission distance is pre-decided, the Tx supply current I_{Tx} can also be calculated accordingly.

Since the maximum distance keeping the Rx circuit working is changed with $I_{Tx}(t)$ with a relationship close to the square root. So, in order to increase VLC effective
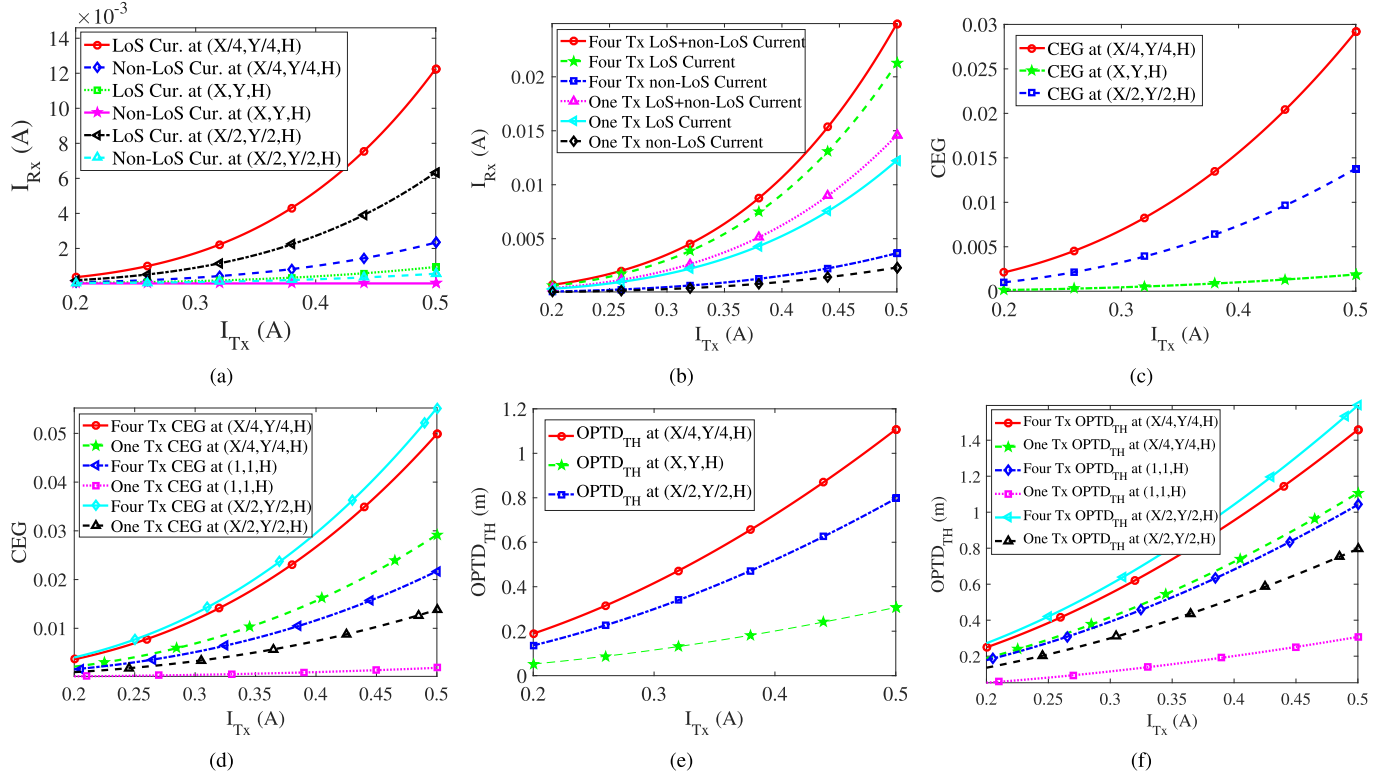
Fig. 9. The dynamic responses and parameters with one or four Txs. (a) is the I_{Rx} with one Tx at $(X/4, Y/4, Z)$. (b) is the I_{Rx} with one Tx at $(X/4, Y/4, Z)$ and four Txs. (c) is the CEG with one Tx at $(X/4, Y/4, Z)$. (d) is the CEG with one Tx at $(X/4, Y/4, Z)$ and four Txs. (e) is the OPTD$_{TH}$ with one Tx at $(X/4, Y/4, Z)$. (f) is the OPTD$_{TH}$ with one Tx at $(X/4, Y/4, Z)$ and four Txs.
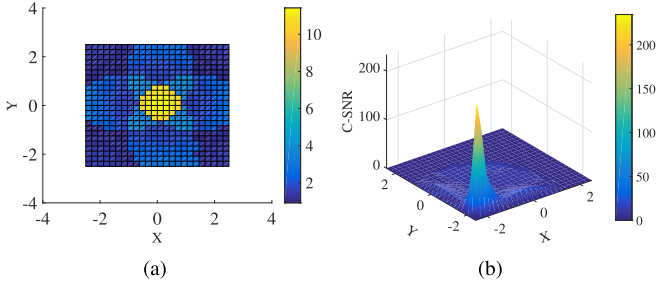

Fig. 10. (a) is the C-SNR with four Txs and (b) is the C-SNR with one Tx.

TABLE IV
CET PARAMETERS WITH DIFFERENT SAMPLE FREQUENCY
AND RELATE POSITIONS

f_s (MHz)	T_p (ns)	Tx	Rx	I_{Tx} (mA)	CEG	C-SNR	$OPT-D_{TH}$ (m)	Status
100	10	$0, 0, 0$	X, Y, H	500	0.17	13	1.56	Y
100	10	$X/2, Y/2, Z/2$	$X/2, Y/2, H/2$	500	0.27	32	2.30	Y
200	5	$0, 0, 0$	X, Y, H	500	0.18	0.8	1.56	N
200	5	$X/2, Y/2, Z/2$	$X/2, Y/2, H/2$	500	0.29	1.3	2.30	Y
100	10	$0, 0, 0$	X, Y, H	100	0.17	13	0.87	N
100	10	$X/2, Y/2, Z/2$	$X/2, Y/2, H/2$	100	0.29	32	1.42	N

communication distance, only increasing Tx current value is not as directly efficient as expected because of the square relationship.

The signal or noise current responses are important for VLC system performance evaluation. Let signal frequency $f_s = 125$ MHz, then $T_p = 8$ ns. If current at the Rx after $1/((f_s \cdot c) + d_0/c)$ time delay, it would become noise current. Four Txs C-SNR is calculated by (26), as shown in Fig. 10(a). When the Rx is at $(X/4, Y/4, H)$ and Tx is at $(X/4, Y/4, Z)$, static C-SNR is shown in Fig. 10(b). The peak C-SNR value appears around the room corner. That is because of the noise optical power is much smaller than signal optical power at the room corner. While, at $(X/4, Y/4, H)$, there still exists much noise optical power. So C-SNR does not appear the maximum value at $(X/4, Y/4, H)$.

Based on the above calculations and diagrams, the induced Rx current is tightly affected by the relative position between

the Tx and Rx. LoS case has the best response for one Tx case. But if Tx number increases, the Rx induced current would be interfered by LoS optical power from other Txs. That would cause Rx ISI problems. Enlarging the relative positions between Txs would be useful for ISI problem. To avoid inter-disturbing, the safe distance conditions between Txs can be calculated based on the time delay $1/(f_s \cdot c) + d_0/c$ and H parameters. To help to detect the signals from re-generated current, the Rx hardware amplifier and de-noise circuit need to be carefully designed. C-SNR parameter is important for the design of Rx amplifier circuits and noise reduction circuits. C-SNR depends on signal generation frequency and the relative position between the Tx and Rx. Simulation results

are shown in Table IV with various frequency and position settings. Here, status means whether $I_{Rx} \geq I_{Rx\_L}$.

V. CONCLUSIONS

This paper has evaluated VLC system based on both hardware circuit and optical parameters. By exploiting the potential relationships among the Tx's hardware supply current, radiant optical power, and the Rx's re-generated current, the current energy transmission characteristics have been analyzed theoretically. An innovate CETCM model has been built up based on the analyses. It makes clear the basic working mechanism and calculation equations of the VLC system from Tx driving current to Rx induced current energy. Four CET parameters have been proposed accordingly. They are peak current energy responses, current energy gain, threshold of optical power transferring distance, and current signal-to-noise ratio. Based on CETCM and CET parameters, simulations have been carried out with various distances, Tx driving current, signal sample frequencies, and Rx/Tx positions. Experiments show that current energy gain is less than 5% because of serious radiant optical power transmission and conversion lost. In the scenario of four Txs and one Tx VLC system with 500 mA Tx supply current, the optical power transferring distances reach to about 1.5 m and 1.1 m which can successfully re-generate minimum Rx current. C-SNR has the maximum value at the center position in four Txs case. However, ISI is still a critical problem which is related with Txs signal frequency and supply current energy. So, the proposed CETCM and CET parameters can direct the design of VLC system, and these are practical, valuable and efficient methods for VLC system evaluations.

REFERENCES

[1] D. Tsonev, S. Videv, and H. Haas, "Light fidelity (Li-Fi): Towards all-optical networking," *Proc. SPIE, Int. Soc. Opt. Eng.*, vol. 9007, no. 5, p. 900702, 2013.

[2] P. H. Pathak, X. Feng, P. Hu, and P. Mohapatra, "Visible light communication, networking, and sensing: A survey, potential and challenges," *IEEE Commun. Surveys Tuts.*, vol. 17, no. 4, pp. 2047–2077, 4th Quart., 2015.

[3] *IEEE Standard for Local and Metropolitan Area Networks—Part 15.7: Short-Range Wireless Optical Communication Using Visible Light*, IEEE Standard 802.15.7–2011, Sep. 2011, pp.1–309.

[4] Y. Zhou, S. Liang, S. Chen, X. Huang, and N. Chi, "2.08Gbit/s visible light communication utilizing power exponential pre-equalization," in *Proc. WOCC*, Chengdu, China, May 2016, pp. 1–3.

[5] Y. Wang, L. Tao, X. Huang, J. Shi, and N. Chi, "8-Gb/s RGBY LED-based WDM VLC system employing high-order CAP modulation and hybrid post equalizer," *IEEE Photon. J.*, vol. 7, no. 6, Dec. 2015, Art. no. 7904507.

[6] X. Huang, J. Shi, J. Li, Y. Wang, and N. Chi, "A Gb/s VLC transmission using hardware preequalization circuit," *IEEE Photon. Technol. Lett.*, vol. 27, no. 18, pp. 1915–1918, Sep. 15, 2015.

[7] X. Huang *et al.*, "2.0-Gb/s Visible light link based on adaptive bit allocation OFDM of a single phosphorescent white LED," *IEEE Photon. J.*, vol. 7, no. 5, Oct. 2015, Art. no 7904008.

[8] Y. Wang *et al.*, "875-Mb/s asynchronous Bi-directional 64QAM-OFDM SCM-WDM transmission over RGB-LED-based visible light communication system," in *Proc. Opt. Fiber Commun. Conf./Nat. Fiber Opt. Eng.*, Anaheim, CA, USA, 2013, p. OTh1G.3.

[9] F. Che, L. Wu, B. Hussain, X. Li, and C. Yue, "A fully integrated IEEE 802.15.7 visible light communication transmitter with on-chip 8-W 85% efficiency boost LED driver," *J. Lightw. Technol.*, vol. 34, no. 10, pp. 2419–2430, May 2016.

[10] P. A. Haigh *et al.*, "A 10 Mb/s visible light communication system using a low bandwidth polymer light-emitting diode," in *Proc. CSNDSP*, Manchester, U.K., Jul. 2014, pp. 999–1005.

[11] C.-W. Hsu, C.-W. Chow, I.-C. Lu, Y.-L. Liu, C.-H. Yeh, and Y. Liu, "High speed imaging 3×3 MIMO phosphor white-light LED based visible light communication system," *IEEE Photon. J.*, vol. 8, no. 6, Dec. 2016, Art. no. 7907406.

[12] A. Sewaiwar, P. P. Han, and Y. H. Chung, "3-Gbit/s indoor visible light communications using optical diversity schemes," *IEEE Photon. J.*, vol. 7, no. 6, Dec. 2015, Art. no. 7904609.

[13] B. Fahs, A. J. Chowdhury, and M. M. Hella, "A 12-m 2.5-Gb/s lighting compatible integrated receiver for OOK visible light communication links," *J. Lightw. Technol.*, vol. 34, no. 16, pp. 3768–3775, Aug. 15, 2016.

[14] M. Z. Afgani, H. Haas, H. Elgala, and D. Knipp, "Visible light communication using OFDM," in *Proc. TRIDENTCOM*, Mar. 2006, p. 134.

[15] J. M. Kahn and J. R. Barry, "Wireless infrared communications," *Proc. IEEE*, vol. 85, no. 2, pp. 265–298, Feb. 1997.

[16] Y. Wang and N. Chi, "Demonstration of high-speed 2×2 non-imaging MIMO Nyquist single carrier visible light communication with frequency domain equalization," *J. Lightw. Technol.*, vol. 32, no. 11, pp. 2087–2093, Jun. 1, 2014.

[17] H. Chun *et al.*, "Brien, and H. Haas, "LED based wavelength division multiplexed 10 Gb/s visible light communications," *J. Lightw. Technol.*, vol. 34, no. 13, pp. 3047–3052, Jul. 1, 2016.

[18] K. Lee, H. Park, and J. R. Barry, "Indoor channel characteristics for visible light communications," *IEEE Commun. Lett.*, vol. 15, no. 2, pp. 217–219, Feb. 2011.

[19] X. Chen and M. Jiang, "Adaptive statistical Bayesian MMSE channel estimation for visible light communication," *IEEE Trans. Signal Process.*, vol. 65, no. 5, pp. 1287–1299, Mar. 2017.

[20] C. He, T. Q. Wang, and J. Armstrong, "Performance of optical receivers using photodetectors with different fields of view in a MIMO ACO-OFDM system," *J. Lightw. Technol.*, vol. 33, no. 23, pp. 4957–4967, Dec. 1, 2015.

[21] A. Nuwanpriya, S.-W. Ho, and C. S. Chen, "Indoor MIMO visible light communications: Novel angle diversity receivers for mobile users," *IEEE J. Sel. Areas Commun.*, vol. 33, no. 9, pp. 1780–1792, Sep. 2015.

[22] Y. Hong, T. Wu, and L.-K. Chen, "On the performance of adaptive MIMO-OFDM indoor visible light communications," *IEEE Photon. Technol. Lett.*, vol. 28, no. 8, pp. 907–910, Apr. 15, 2015.

[23] L. Wei, H. Zhang, and J. Song, "Experimental demonstration of a cubic-receiver-based MIMO visible light communication system," *IEEE Photon. J.*, vol. 9, no. 1, Feb. 2017, Art. no. 7900107.

[24] A. Al-Kinani, C.-X. Wang, H. Haas, and Y. Yang, "A geometry-based multiple bounce model for visible light communication channels," in *Proc. IEEE IWCMC*, Paphos, Cyprus, Sep. 2016, pp. 31–37.

[25] A. Al-Kinani, C.-X. Wang, H. Haas, and Y. Yang, "Characterization and modeling of visible light communication channels," in *Proc. IEEE 83rd Veh. Technol. Conf. (VTC Spring)*, Nanjing, China, May 2016, pp. 1–5.

[26] S. Ma, R. Yang, H. Li, Z. L. Dong, H. Gu, and S. Li, "Achievable rate with closed-form for SISO channel and broadcast channel in visible light communication networks," *J. Lightw. Technol.*, vol. 35, no. 14, pp. 2778–2787, Jul. 15, 2017.

[27] S. Ma, T. Zhang, S. Lu, H. Li, Z. Wu, and S. Li, "Energy efficiency of SISO and MISO in visible light communication systems," *J. Lightw. Technol.*, to be published.

[28] H. Elgala, R. Mesleh, and H. Haas, "Indoor broadcasting via white LEDs and OFDM," *IEEE Trans. Consum. Electron.*, vol. 55, no. 3, pp. 1127–1134, Aug. 2009.

[29] A. H. Azhar, T. Tran, and D. O'Brien, "A gigabit/s indoor wireless transmission using MIMO-OFDM visible-light communications," *IEEE Photon. Technol. Lett.*, vol. 25, no. 2, pp. 171–174, Jan. 15, 2013.

[30] Q. Wang, Z. Wang, and L. Dai, "Multiuser MIMO-OFDM for visible light communications," *IEEE Photon. J.*, vol. 7, no. 6, pp. 1–11, Dec. 2015.

[31] F. Yang, J. Gao, and S. Liu, "Novel visible light communication approach based on hybrid OOK and ACO-OFDM," *IEEE Photon. Technol. Lett.*, vol. 28, no. 14, pp. 1585–1588, Jul. 15, 2016.

[32] Y. Yang, Z. Zeng, J. Cheng, and C. Guo, "An enhanced DCO-OFDM scheme for dimming control in visible light communication systems," *IEEE Photon. J.*, vol. 8, no. 3, pp. 1–13, Jun. 2016.

[33] M. S. A. Mossaad, S. Hranilovic, and L. Lampe, "Visible light communications using OFDM and multiple LEDs," *IEEE Trans. Commun.*, vol. 63, no. 11, pp. 4303–4304, Nov. 2015.

[34] R. Feng, M. Dai, H. Wang, B. Chen, and X. Lin, "Linear precoding for multiuser visible-light communication with field-of-view diversity," *IEEE Photon. J.*, vol. 8, no. 2, Apr. 2016, Art. no. 7902708.

[35] X. Liu, C. Gong, S. Li, and Z. Xu, "Signal characterization and receiver design for visible light communication under weak illuminance," *IEEE Commun. Lett.*, vol. 20, no. 7, pp. 1349–1352, Jul. 2016.

[36] L. Yin, W. O. Popoola, X. Wu, and H. Haas, "Performance evaluation of non-orthogonal multiple access in visible light communication," *IEEE Trans. Commun.*, vol. 64, no. 12, pp. 5162–5175, Dec. 2016.

[37] C.-H. Yeh, C.-W. Chow, H.-Y. Chen, Y.-L. Liu, and D.-Z. Hsu, "Investigation of phosphor-LED lamp for real-time half-duplex wireless VLC system," *J. Opt.*, vol. 18, no. 6, p. 065701, 2016.

[38] M. Bessho and K. Shimizu, "Latest trends in LED lighting," *Electron. Commun. Jpn.*, vol. 95, no. 1, pp. 1–7, 2012.

[39] *NCSWE17A Product Datasheet*. Accessed: Apr. 20, 2018. [Online]. Available: http://www.nichia.co.jp/en/product/led_product_data.html?type=%27NCSWE17A%27

[40] *C513A Product Datasheet*. Accessed: Apr. 20, 2018. [Online]. Available: http://www.marktechopto.com/pdf/products/datasheet/C513A-WSN_WSS_MSN_MSS.pdf

[41] J. C. Daly, "Fiber optic intermodulation distortion," *IEEE Trans. Commun.*, vol. COM-30, no. 8, pp. 1954–1958, Aug. 1982.

[42] I. Neokosmidis, T. Kamalakis, J. W. Walewski, B. Inan, and T. Sphicopoulos, "Impact of nonlinear LED transfer function on discrete multitone modulation: Analytical approach," *J. Lightw. Technol.*, vol. 27, no. 22, pp. 4970–4978, Nov. 15, 2009.

[43] T.-P. Sun and C.-H. Wang, "Specially designed driver circuits to stabilize LED light output without a photodetector," *IEEE Trans. Power Electron.*, vol. 27, no. 9, pp. 4140–4152, Sep. 2012.

[44] G. Wyszecki and W. S. Stiles, *Color Science: Concepts and Methods, Quantitative Data and Formulae*, 2nd ed. Hoboken, NJ, USA: Wiley, 1982.

[45] D. A. Tsonev, "High speed energy efficient incoherent optical wireless communications," Ph.D. dissertation, School Eng., Univ. Edinburgh, Scotland, U.K., Jun. 2015.

[46] A. Mirvakili, "Development of LED driver circuit architectures for future generation visible smart lighting networks combining high-speed data communication and illumination control," Ph.D. dissertation, Dept. Elect. Eng., Tufts Univ., Medford, MA, USA, Feb. 2015.

[47] T. Cevik and S. Yilmaz, "An overview of visible light communication systems," *Int. J. Comput. Netw. Commun.*, vol. 7, no. 6, pp. 139–150, 2015.

[48] X. Ning, R. Winston, and J. O. Gallagher, "Dielectric totally internally reflecting concentrators," *Appl. Opt.*, vol. 26, no. 2, pp. 300–305, Jan. 1987.

[49] *LSSPD-1.2 Lightsensing Product Datasheet*. Accessed: Apr. 20, 2018. [Online]. Available: http://www.lightsensing.com/upfile/2017-06/20170616535.pdf

[50] *602PX First Sensor Product Datasheet*. Accessed: Apr. 20, 2018. [Online]. Available: http://www.first-sensor.com/cms/upload/appnotes/application-note-pin.pdf

[51] D. A. Luong, T. C. Thang, and A. T. Pham, "Effect of avalanche photodiode and thermal noises on the performance of binary phase-shift keying-subcarrier-intensity modulation/free-space optical systems over turbulence channels," *IET Commun.*, vol. 7, no. 8, pp. 738–744, Mar. 2013.

[52] K. J. Williams and R. D. Esman, "Observation of photodiode nonlinearities," *Electron. Lett.*, vol. 28, no. 8, pp. 731–732, Apr. 1992.

[53] P.-L. Liu, K. J. Williams, M. Y. Frankel, and R. D. Esman, "Saturation characteristics of fast photodetectors," *IEEE Trans. Microw. Theory Techn.*, vol. 47, no. 7, pp. 1297–1303, Jul. 1999.

[54] K. J. Williams, R. D. Esman, and M. Dagenais, "Effects of high space-charge fields on the response of microwave photodetectors," *IEEE Photon. Technol. Lett.*, vol. 6, no. 5, pp. 639–641, May 1994.

[55] K. J. Williams and R. D. Esman, "Design considerations for high-current photodetectors," *J. Lightw. Technol.*, vol. 17, no. 8, pp. 1443–1454, Aug. 1999.

[56] C. Gong, S. Li, Q. Gao, and Z. Xu, "Power and rate optimization for visible light communication system with lighting constraints," *IEEE Trans. Signal Process.*, vol. 63, no. 16, pp. 4245–4256, Aug. 2015.

[57] G. P. Agrawal, *Fiber–Optic Communication Systems*, 3rd ed. Hoboken, NJ, USA: Wiley, 2002.

[58] Z. Ghassemlooy, W. Popoola, and S. Rajbhandari, *Optical Wireless Communications: System and Channel Modelling With MATLAB*. Boca Raton, FL, USA: CRC Press, 2013.

[59] N. Chi, *Key Devices and Applications of LED Visible Light Communication*, 1st ed. Beijing, China: Posts & Telecom Press, Aug. 2015.

[60] T. Komine and M. Nakagawa, "Fundamental analysis for visible-light communication system using LED lights," *IEEE Trans. Consum. Electron.*, vol. 50, no. 1, pp. 100–107, Feb. 2004.

[61] D. A. Tulchinsky, X. Li, N. Li, S. Demiguel, J. C. Campbell, and K. J. Williams, "High-saturation current wide-bandwidth photodetectors," *IEEE J. Sel. Topics Quantum Electron.*, vol. 10, no. 4, pp. 702–708, Jul. 2004.

[62] M. Piels, A. Ramaswamy, and J. E. Bowers, "Nonlinear modeling of waveguide photodetectors," *Opt. Exp.*, vol. 21, no. 13, pp. 15634–15644, 2013.

[63] J. B. Carruthers and S. M. Carroll, "Statistical impulse response models for indoor optical wireless channels," *Int. J. Commun. Syst.*, vol. 8, no. 3, pp. 267–284, 2005.

[64] J. B. Carruthers and P. Kannan, "Iterative site-based modeling for wireless infrared channels," *IEEE Trans. Antennas Propag.*, vol. 50, no. 5, pp. 759–765, May 2002.

[65] T. Wang, Y. A. Sekercioglu, and J. Armstrong, "Analysis of an optical wireless receiver using a hemispherical lens with application in MIMO visible light communications," *J. Lightw. Technol.*, vol. 31, no. 11, pp. 1744–1754, Jun. 1, 2013.

Li Zhou received the B.Sc. and M.E. degrees in electrical engineering from Shandong University, China, in 1998 and 2001, respectively, and the Ph.D. degree in electrical engineering from Zhejiang University, Hangzhou, China, in 2004. She was a Project Manager with the Freescale Semiconductor Research and Development Center until 2009. Since 2009, she has been an Assistant Professor with Shandong University. She participated in multiple National High-Technology SoC and HDTV Fundamental Research projects, led multiple 65/90 nm 10 million gate scale VLSI SoC chips, and joined many VLSI projects and architecture research. Her current research interests include visible-light communication system design and evaluations, video processing system and hardware design, GPU architecture and VLSI design, and embedded systems and ASIC design.

Cheng-Xiang Wang (S'01–M'05–SM'08–F'17) received the B.Sc. and M.Eng. degrees in communication and information systems from Shandong University, China, in 1997 and 2000, respectively, and the Ph.D. degree in wireless communications from Aalborg University, Denmark, in 2004.

He was a Research Assistant with the Hamburg University of Technology, Hamburg, Germany, from 2000 to 2001, a Research Fellow at the University of Agder, Grimstad, Norway, from 2001 to 2005, and a Visiting Researcher with Siemens AG-Mobile Phones, Munich, Germany, in 2004. He has been with Heriot-Watt University, Edinburgh, U.K., since 2005, and became a Professor in wireless communications in 2011. He is also an Honorary Fellow at The University of Edinburgh, U.K., a Chair Professor of Shandong University, and a Guest Professor of Southeast University, China. He has co-authored two books, one book chapter, and over 320 papers in refereed journals and conference proceedings. His current research interests include wireless channel measurements/modeling and (B)5G wireless communication networks, including green communications, cognitive radio networks, high mobility communication networks, massive MIMO, millimeter wave communications, and visible-light communications.

Dr. Wang is a fellow of the IET and HEA. He received nine best paper awards from the IEEE GLOBECOM 2010, the IEEE ICCT 2011, ITST 2012, the IEEE VTC 2013-Spring, IWCMC 2015, IWCMC 2016, IEEE/CIC ICCC 2016, and WPMC 2016. He has served as a technical program committee (TPC) member, the TPC chair, and a general chair for over 80 international conferences. He has served as an Editor for nine international journals, including the IEEE TRANSACTIONS ON WIRELESS COMMUNICATIONS from 2007 to 2009, the IEEE TRANSACTIONS ON VEHICULAR TECHNOLOGY since 2011, and the IEEE TRANSACTIONS ON COMMUNICATIONS since 2015. He was a Lead Guest Editor of the IEEE JOURNAL ON SELECTED AREAS IN COMMUNICATIONS Special Issue on Vehicular Communications and Networks. He was also a Guest Editor of the IEEE JOURNAL ON SELECTED AREAS IN COMMUNICATIONS Special Issue on Spectrum and Energy Efficient Design of Wireless Communication Networks and Special Issue on Airborne Communication Networks, and the IEEE TRANSACTIONS ON BIG DATA Special Issue on Wireless Big Data. He is recognized as a Web of Science 2017 Highly Cited Researcher.

Ahmed Al-Kinani received the B.Sc. degree (Hons.) in laser physics and the M.Sc. degree in optical communications from the University of Technology, Baghdad, Iraq, in 2001 and 2004, respectively, and the Ph.D. degrees from The University of Edinburgh and Heriot-Watt University, Edinburgh, U.K., in 2018. He is currently with the Iraqi Ministry of Communications, Baghdad, Iraq, as a Senior Programmer. His main research interests include wireless channel characterization and modeling for VLC.

Wen-Sheng Zhang received the M.E. degree in electrical engineering from Shandong University, China, in 2005, and the Ph.D. degree in electrical engineering from Keio University, Japan, in 2011. In 2011, he joined the School of Information Science and Engineering, Shandong University, where he is currently an Associate Professor. His research interests include cognitive radio networks, random matrix theory, and visible-light communications.